Received: 27 November 2021 | Revised: 6 January 2022 | Accepted: 27 January 2022

DOI: 10.1002/cne.25308

RESEARCH ARTICLE

JCN RESEARCH IN SYSTEMS NEUROSCIENCE THE JOURNAL OF COMPARATIVE NEUROLOGY WILEY

Digital reconstruction and quantitative morphometric analysis of bipolar cells in live rat retinal slices

Rémi Fournel | Margaret L. Veruki | Espen Hartveit

Department of Biomedicine, University of Bergen, Bergen, Norway

Correspondence
Espen Hartveit, Department of Biomedicine, University of Bergen, Jonas Lies vei 91, N-5009 Bergen, Norway.
Email: espen.hartveit@biomed.uib.no

Funding information
European Union's Horizon 2020 research and innovation program under the Marie Skłodowska-Curie grant agreement, Grant/Award Number: 674901; Norges Forskningsråd, Grant/Award Numbers: 182743 (EH), 189662 (EH), 214216 (EH), 261914 (MLV); Horizon 2020 Framework Programme, Grant/Award Number: 674901

Abstract

Bipolar cells convey signals from photoreceptors in the outer retina to amacrine and ganglion cells in the inner retina. In mammals, there are typically 10–15 types of cone bipolar cells and one type of rod bipolar cell. Different types of cone bipolar cells are thought to code and transmit different features of a complex visual stimulus, thereby generating parallel channels that uniquely filter and transform the photoreceptor outputs. Differential synaptic connectivity and expression of ligand- and voltage-gated ion channels are thought to be important mechanisms for processing and filtering visual signals. Whereas the biophysical basis for such mechanisms has been investigated more extensively in rat retina, there is a lack of quantitative morphological data necessary for advancing the structure–function correlation in this species, as recent connectomics investigations have focused on mouse retina. Here, we performed whole-cell recordings from cone and rod bipolar cells in rat retinal slices, filled the cells with fluorescent dyes, and acquired image stacks by multiphoton excitation microscopy. Following deconvolution, we performed digital reconstruction and morphometric analysis of 25 cone and 14 rod bipolar cells. Compared to previous descriptions, the extent and complexity of branching of the axon terminal was surprisingly high. By precisely quantifying the level of stratification of the axon terminals in the inner plexiform layer, we have generated a reference system for reliable classification of individual cells in future studies focused on correlating physiological and morphological properties. The implemented workflow can be extended to the development of morphologically realistic compartmental models for these neurons.

KEYWORDS
branching pattern, cone bipolar cells, dendrites, digital reconstruction, morphometry, retina

1 | INTRODUCTION

A basic tenet of neurobiology is that structure is inextricably linked to function. This has inspired numerous attempts at characterization and classification of the complete morphology of neurons in different regions of the central nervous system. The ability to acquire and analyze complete neuronal morphologies has advanced with continuous technological developments since the time of Golgi (1873) and Cajal (1894), with progressive refinements and increased understanding of the anatomical details of different types of neurons.

Retinal bipolar cells are short-range projection neurons that link the outer and inner retina. Their dendrites contact and receive input from the terminals of photoreceptors and horizontal cells in the outer plexiform layer (OPL) and their axons descend through the inner nuclear and

inner plexiform layers (INL and IPL), with their axon terminals stratifying at different levels of the IPL (reviewed by Euler et al., 2014). The stratification level of the axon terminals of different bipolar cells in the IPL determines their synaptic connectivity (e.g., Strettoi et al., 2010) and is an important basis for the morphological classification of different types of bipolar cells (Cajal, 1893, 1894). The fundamental distinction between rod and cone bipolar cells was clearly recognized by Cajal (1893, 1894), with the two types receiving input from rod and cone photoreceptors, respectively (Dowling & Boycott, 1966). Whereas there is only a single type of rod bipolar cell, which transmits signals primarily to two types of amacrine cells in the IPL, there are 10–15 different types of cone bipolar cells, which transmit signals to a large number of different types of amacrine and ganglion cells in the IPL. Different types of cone bipolar cells are thought to be responsible for generating and transmitting different visual responses, such that different cell types constitute specific and parallel channels that filter and transform the photoreceptor output in unique ways (e.g., Ichinose et al., 2014; for review, see Euler et al., 2014).

Data for morphology and classification of bipolar cells have been obtained with several light microscopic techniques, including Golgi impregnation (Boycott & Dowling, 1969; Boycott & Wässle, 1991; Cajal, 1893, 1894, 1911; Dacheux & Raviola, 1986; Famiglietti, 1981; Linberg et al., 1996; MacNeil et al., 2004; Polyak, 1941; West, 1976, 1978), injection of tracers like biocytin and Neurobiotin (Euler & Wässle, 1995; Oltedal et al., 2009), injection of fluorescent dyes (Euler & Wässle, 1995; Ghosh et al., 2004; Hartveit, 1997; Ivanova & Müller, 2006), and biolistic ("gene gun") transfer of fluorescent dyes (Pignatelli & Strettoi, 2004). The morphological analysis of bipolar cells injected with fluorescent dyes has been improved by the increased spatial resolution offered by confocal microscopy (Ghosh et al., 2004; Haverkamp et al., 2008; Hellmer et al., 2016; Light et al., 2012; Pignatelli & Strettoi, 2004; Vielma & Schmachtenberg, 2016). In parallel with light microscopic investigations, bipolar cell morphology and classification have been investigated at the ultrastructural level, using serial section reconstruction based on transmission electron microscopy (EM); Cohen & Sterling, 1990; McGuire et al., 1984; Sterling, 1983; Tsukamoto & Omi, 2015, 2017; Tsukamoto et al., 2001 or, more recently, serial block face scanning EM (SBFSEM; Behrens et al., 2016; Greene et al., 2016; Helmstaedter et al., 2013).

The need for high spatial resolution is underscored by the recent discovery of new types of cone bipolar cells when complete reconstructions at the ultrastructural level were performed for relatively large volumes of the mouse retina (Helmstaedter et al., 2013). First, such investigations allowed a more precise determination of the level of axon terminal stratification in the IPL, suggesting that some previously accepted bipolar cell types were actually composed of more than one type (Greene et al., 2016; Helmstaedter et al., 2013). Second, because such "deep connectomics" investigations are able to provide complete reconstruction of all neuronal arbors within a given volume, the classification of types can be aided by the observation of potential "tiling violations" among the axon terminals, suggesting that individual cells belong to different types that tile the retina independently of each other.

Although morphology correlates with and predicts some functional properties, it does not predict every functional property. This means that morphological characterization and classification must be combined with physiological investigations. Functional imaging studies have verified that different types of cone bipolar cells display different visual response properties (Franke et al., 2017), but the mechanisms that are responsible for generating these differences are mostly unknown. To investigate such mechanisms, electrophysiological recording from single neurons is still unsurpassed with respect to resolution and specificity, but does not by itself provide the morphological information necessary to correlate structure and function. Whereas several studies have used wide-field or confocal fluorescence microscopy to characterize the morphology following whole-cell electrophysiological recording in slices, it is a challenge that the morphological classification tends to be qualitative and based on illustrations of "typical" cells. Therefore, it can often be difficult to classify any individual cell based on morphology and axon terminal stratification when it is similar to two (or more) types with overlapping levels of stratification in the IPL.

It is a disadvantage that the recent high-resolution structural maps lack information about important functional properties, for example, passive membrane properties that determine the electrotonic characteristics of neurons. It is also difficult to see how such deep connectomics studies can be extended to a workflow incorporating compartmental modeling, where physiological measurements are made on the same cells used for morphological reconstruction. This raises the question whether the morphological classification of electrophysiologically recorded cells can be made more precise by imaging with multiphoton excitation (MPE) and infrared laser scanning gradient contrast (IR-LSGC) microscopy. This provides images of both fluorescence and retinal landmarks (e.g., borders between retinal layers) and can be used for accurate, quantitative morphological reconstruction. Here, we present a characterization of the morphological properties of different types of rat retinal bipolar cells, with a focus on soma size, dendritic tree size and structure, and axon terminal branching and stratification. All imaging was performed by MPE microscopy during patch-clamp recording from visually targeted neurons in slices. The choice of rat retina was motivated by the more extensive knowledge of biophysical mechanisms and physiological properties of bipolar cells in this species compared to, for example, mouse. A major goal was to implement a workflow that can be extended to the development of morphologically realistic compartmental models for these neurons.

2 | MATERIALS AND METHODS

2.1 | Retinal slice preparation

General aspects of the methods have previously been described in detail (Zandt et al., 2017). The use of animals in this study was carried out under the approval of and in accordance with the Animal Laboratory Facility at the Faculty of Medicine at the University of Bergen (accredited by AAALAC International). Male and female albino rats (Wistar HanTac, bred in-house or purchased from Taconic Biosciences [Denmark]; 4–7 weeks postnatal) had ad libitum access to food and water and were kept on a 12/12 light/dark cycle. Under normal room

illumination, animals were deeply anaesthetized with isoflurane (IsoFlo vet 100%; Abbott Laboratories Ltd., Maidenhead, UK) in 100% O_2 and killed by cervical dislocation. After dissecting the retina, vertical retinal slices were cut by hand and visualized with MPE microscopy using a custom-modified "Movable Objective Microscope" (MOM; Sutter Instrument, Novato, CA, USA) with a ×20 water immersion objective (XLUMPLFL; NA = 0.95; Olympus) and infrared Dodt gradient contrast videomicroscopy (IR-DGC), using an IR-sensitive analog CCD camera (VX55; TILL Photonics, Gräfelfing, Germany). All recordings were carried out at room temperature (22 –25°C).

2.2 | Solutions and drugs

The standard extracellular perfusing solution was continuously bubbled with 95% O_2–5% CO_2 and had the following composition (in mM): 125 NaCl, 25 $NaHCO_3$, 2.5 KCl, 2.5 $CaCl_2$, 1 $MgCl_2$, 10 glucose, and pH 7.4. The recording pipettes were filled with an intracellular solution of the following composition (in mM): 125 K-gluconate, 5 KCl, 8 NaCl, 10 Hepes, 0.2 EGTA, 4 MgATP, and 0.4 Na_3GTP (pH adjusted to 7.3 with KOH). The pipette solution also contained Alexa Fluor 594 hydrazide as sodium salt (40 or 60 μM; Invitrogen/Thermo Fisher Scientific; henceforth referred to as Alexa 594). For one cell, the pipette solution contained Lucifer yellow (1 mg/ml) instead of Alexa 594. The osmolality was ~290 mOsmol · kg^{-1} H_2O.

2.3 | Whole-cell recording

Patch pipettes were pulled from thick-walled borosilicate glass (outer diameter, 1.5 mm; inner diameter, 0.86 mm). The open-tip resistance of the pipettes (R_{pip}) ranged from 7 to 10 MΩ when filled with intracellular solution. Whole-cell voltage-clamp recordings were performed with an EPC10-triple or an EPC10-USB-dual (RRID: SCR_018399) amplifier (HEKA Elektronik, Lambrecht/Pfalz, Germany) controlled by Patchmaster software (RRID: SCR_000034). To keep the background fluorescence in the area immediately surrounding the cell body to a minimum, only a small positive pressure (5–10 mbar) was applied to the pipette as it approached the cell. After making a GΩ-seal (≥ 2 GΩ), the whole-cell recording configuration was established by a combination of brief electrical pulses and negative pressure pulses.

2.4 | Image acquisition for MPE microscopy and deconvolution

For MPE microscopy, fluorescence from neurons filled with Alexa 594 was imaged with the MOM equipped with a mode-locked Ti:sapphire laser (Mai Tai DeepSee; Spectra-Physics) tuned to 810 nm. For the cell filled with Lucifer yellow, the laser was tuned to 850 nm. Scanning was performed by galvanometric scanners (XY; Cambridge Technology), fluorescence was detected by multialkali photomultiplier tubes (R6357; Hamamatsu Corp.), and the analog signals were digitized by an acquisition board (PXIe-6356, National Instruments). The intensity of the laser was attenuated and controlled by an electro-optic modulator (350-80LA with BK option; ConOptics). During image acquisition, exposure to IR laser light was controlled by an electronic shutter (LS6ZM2; Vincent Associates), thereby minimizing the total exposure time. An image stack was acquired as a series of optical sections (1024 × 1024 pixels) with XY pixel size ~70 to ~80 nm (depending on the magnitude of the digital zoom factor) and collected at a focal plane interval (ΔZ) of 0.4 μm (for one cell, the image stack was acquired at 512 × 512 pixels). For each image stack, we acquired two channels, and at each focal plane, two images were averaged on-line. The first channel sampled the fluorescence light as described above. The second channel was used for IR-LSGC (Yasuda et al., 2004) and sampled the forward-scattered IR laser light after it passed the substage condenser and a Dodt gradient contrast tube (Luigs & Neumann, Ratingen, Germany). MPE microscopy and image acquisition were controlled by ScanImage software (versions 3.8.1 and 2018) running under Matlab (The Mathworks).

To ensure that the distal processes of bipolar cells were adequately filled with dye, acquisition of an image stack typically started 10–12 min after establishing the whole-cell recording configuration. The physiological condition of the cell was monitored by recording the holding current and input resistance throughout the acquisition period. A complete stack was generally acquired within 20–30 min. In some cases, additional stacks were sampled to take advantage of the enhanced fluorescence intensity obtained in the thin dendritic processes after a longer period of filling the cell with dye. Deconvolution of MPE image stacks for morphological reconstruction was performed with Huygens software (version 14, 64 bit; Scientific Volume Imaging; RRID: SCR_014237), as described in Zandt et al. (2017). Following deconvolution, the image stacks were also processed with the "stabilization" tool in Huygens that corrected (aligned) any slices in the image stack to compensate for movement and drift (in the XY plane) during acquisition.

2.5 | Three-dimensional digital reconstruction

Quantitative morphological reconstruction of the fluorescently labeled cells was done manually with Neurolucida 360 software (versions 2017–2020, 64 bit; MBF Bioscience, Williston, VT, USA; RRID: SCR_016788), for a detailed description, see Zandt et al. (2017). The three-dimensional (3D) reconstruction of the soma was based on manually tracing a single contour around the cell body, at the focal plane where it appeared the largest. As we only imaged live cells, there was no need to correct for errors related to shrinkage. Cells that displayed clear signs of mechanical injury or phototoxicity (visible as "beading" of processes) were not included in the material for reconstruction.

With an excitation wavelength of 810 nm and NA = 0.95 for the objective used, the resolution limit becomes approximately 0.37 μm in the ideal (diffraction-limited) case. Processes that are thinner than this can be detected if the intensity is sufficiently high, but it is not possible

to resolve their true diameter. EM is currently the only reliable source of information when the diameters of the thinnest dendritic and axonal processes are below the light microscopic resolution limit. We, therefore, made measurements from the thinnest (yet clearly discernable) axonal and dendritic processes illustrated in the few published electron micrographs from rat retina. For dendritic processes, we found the minimum diameter to be 0.12 ± 0.02 μm (range 0.10–0.14, $n = 6$ processes, Brandstätter et al., 2004; Cao et al., 2015; Koulen et al., 1997). For processes in the axon terminal, we found the minimum diameter of intervaricosity segments to be 0.15 ± 0.01 μm (range 0.14–0.15, $n = 3$ processes, Chun et al., 1993, 1999; Sassoè-Pognetto et al., 1994). Accordingly, we have, when necessary, constrained the dendrites and axon terminal intervaricosity segments to a minimum diameter of 0.12 and 0.15 μm, respectively.

Even for reconstruction of the thicker axon shafts (see Results for explanations of anatomical terminology), a subjective element is involved when deciding the diameters of processes visualized by imaging cells filled with fluorescent dye (cf. Jaeger, 2001). To guide our judgment, we made measurements from digital image stacks acquired with confocal microscopy of flatmount retinal tissue immunolabeled for protein kinase C (PKC) that is specific for rod bipolar cells (Greferath et al., 1990). The XY plane of the image stack corresponded to the surface of the retina such that in each slice, the axons of rod bipolar cells appeared in cross section as ring-shaped, membrane-associated fluorescent structures surrounding a nonfluorescent center. For three image stacks (acquired from separate quadrants; deconvolved with Huygens), we selected a single slice, located approximately midway between the cell bodies and the axon terminals, and measured transverse intensity profiles (Huygens) of randomly selected axons that were adequately labeled. Each intensity profile passed through the center of the profile and was oriented to follow the smallest diameter if the profile had an oval shape (corresponding to an oblique orientation of the axon relative to the plane of the confocal slice). Each intensity profile was fitted with the sum of two Gaussian functions (MultiPeak Fit package in IGOR Pro; WaveMetrics, Lake Oswego, OR, USA; RRID: SCR_000325) and the axon diameter was estimated as the distance between the locations of the two peaks. For a total of 90 axons (30 axons in each of three slices), the average diameter was 0.77 ± 0.11 (SD) μm (range 0.51–1.05 μm).

Although the measurements from the PKC-labeled retinas could be used as a guide for setting process diameters during reconstruction of rod bipolar cell axons, it cannot be assumed a priori that they can also be used as a guide for cone bipolar cell axons. To compare the thickness of axon shafts of rod and cone bipolar cells, we generated transverse intensity profiles along straight lines oriented perpendicularly to the local longitudinal axis of the axon (Huygens). For each axon, we generated five profiles at approximately equidistant locations between the cell body and the axon terminal, avoiding local extreme values (both maxima and minima) as well as the larger diameters of the most proximal and distal parts where the axon arises from the cell body and transitions to the axon terminal. All intensity profiles were generated from the deconvolved image stacks used for morphological reconstruction and for a given location, the intensity profile was generated from the focal plane (slice) where the width was at its maximum. Each intensity profile was fitted with a Gaussian function (IGOR Pro) and the width was taken as the full width at half-maximum (FWHM), calculated as $SD \times 2^{3/2} \times \sqrt{ln2}$, where SD is the standard deviation obtained from the Gaussian fit. Because the FWHM values of the axons of rod and cone bipolar cells in our material overlapped completely (Figure 1), we used the estimates of axon diameters obtained for immunolabeled rod bipolar cells to guide the reconstruction of both rod and cone bipolar cells.

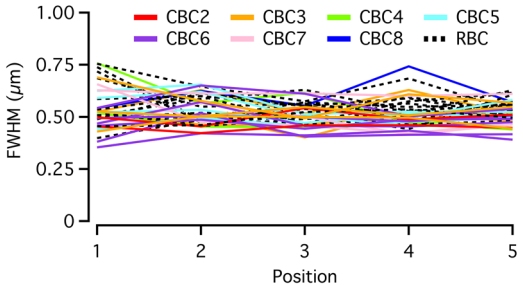

FIGURE 1 Thickness of the axon shafts of cone (CBC2–CBC8) and rod (RBC) bipolar cells at five different positions (with approximately equidistant spacing) from the cell body to the axon terminal (position 1 closest to the cell body, position 5 closest to the axon terminal). For each position, we generated a transverse intensity profile along a straight line (oriented perpendicularly to the local longitudinal axis of the axon) from the deconvolved image stack used for morphological reconstruction. For a given location, the intensity profile was generated from the focal plane (slice), where the width was at its maximum. For each intensity profile, the width was taken as the full width at half-maximum (FWHM), estimated from a Gaussian fit. Notice that the FWHM values for rod and cone bipolar cells completely overlap

2.6 | Detection and reconstruction of axon terminal varicosities

Detection of varicosities was performed manually in Neurolucida 360. A varicosity was defined as a spatially discrete swelling where the maximum diameter increased ≥70% relative to the diameter immediately before and after the swelling, as visualized in the XY plane. In addition, the swelling was classified as a varicosity only if the length of the swelling (as measured along the length of the process) was ≤4 times the diameter of the process before the swelling. We used the "marker" functionality of Neurolucida 360 to indicate the size and location (XYZ) of each varicosity. The size was determined as the diameter of the largest circle that would fit inside the varicosity in the XY plane. The location in Z was determined by the reconstruction point corresponding to the largest diameter of the varicosity. After detection, we used the 3D viewer of Neurolucida 360 to verify that no marker had been misplaced along the Z axis. Subsequently, all markers were "attached" to the corresponding (nearest) part of the axon terminal (using the appropriate functions in Neurolucida 360) to enable analysis in relation to the neuronal arborization.

2.7 | Rotating image stacks and reconstructions in 3D

For illustration purposes, each reconstruction was rotated around the *Z* axis in the plane of the image slice (i.e., around the axis oriented orthogonally to the plane of the image slice) such that the axon was aligned vertically and the retinal layers above and below the reconstructed cell were aligned approximately horizontally. In this way, the *X* axis of the reconstruction was parallel to the retinal layers in the plane of the image slice and the *Y* axis of the reconstruction was perpendicular to the retinal layers in the plane of the image slice.

For purposes of classification and morphometric analysis, it was in several cases necessary to rotate the reconstruction and the associated image stack sampled in the IR-LSGC channel not only around the *Z* axis (as described above), but also around the *X* axis. When the cut surfaces of a slice are not oriented perfectly vertically through the retina, the plane of a bipolar cell axon terminal field (i.e., the plane parallel to the planes defining the retinal layers) becomes tilted relative to the XZ plane of the image stack (as defined during image acquisition). Accordingly, when the axon terminal is projected onto the XY plane, the height (along the *Y* axis) and area of projection (onto the XY plane) become artificially enlarged. The required correction was performed in three steps. In the first step, we determined the required rotation by reading the 3D coordinates of the reconstruction (generated in Neurolucida 360) into IGOR Pro and rotating the cell around the *X* and *Z* axes such that the plane of the axon terminal was aligned parallel to the XZ plane (as judged by eye during simultaneous projection of the reconstruction onto the XY and YZ planes). Often, but not always, this also oriented the axon vertically in both planes (XY and YZ). In the second step, the Neurolucida 360 reconstruction was rotated by the determined angles (around the *X* and *Z* axes), using a combination of Python code and functionality in Neurolucida 360. In the third step, the IR-LSGC image stack was rotated by the same angles (around the *X* and *Z* axes) using functions in Amira (version 2019, FEI SAS/Thermo Fisher Scientific) that aligned the 3D coordinates of the stack with those of the absolute reference system. This was followed by resampling of the transformed stack by interpolation (Lanczos), with preservation of the voxel size from the original stack. The rotated reconstruction and IR-LSGC image stack were then used to analyze the projection onto, and the distribution of the reconstructed processes across, the INL, IPL, and ganglion cell layer (GCL).

2.8 | Quantitative morphological analysis

For general morphological analysis and quantification of dendritic and axonal branching metrics, we used Neurolucida Explorer (versions 2017–2020, 64 bit; MBF Bioscience; RRID: SCR_017348), L-measure (version 5.2; Scorcioni et al., 2008), and IGOR Pro. The single contour used to trace the cell body in the XY plane was used to calculate the perimeter and the Feret maximum and minimum (henceforth termed Feret max and Feret min) of the cell body. Dendritic length was calculated as the total length of all processes from the cell body that projected toward the OPL. A branch segment was defined as the part of a branch between two nodes (branch points) or between a node and a termination point (ending; Capowski, 1989). Thus, the number of segments equals the sum of the number of nodes and the number of termination points. Axon shaft diameter was calculated as the average diameter of the length-weighted segments as follows. First, diameter and length for each segment of the axon shaft were obtained from Neurolucida Explorer. Then, the diameter of each segment was multiplied by its associated length and the values obtained were summed for each axon shaft. The sum was divided by the total length of the axon shaft to obtain the average axon shaft diameter. The 2D convex hull (area) was measured separately for the dendritic tree in the OPL and for the axon terminal in the IPL. In both cases, the 2D convex hull was measured for the projection onto the XZ plane, that is, the surface of the retina, after rotating the reconstruction (as described above). The rotation was identical for measuring the 2D convex hull of the axon terminal and for analyzing the stratification in the IPL. For approximately 50% of the cells, it was necessary to perform a separate rotation when calculating the 2D convex hull of the dendritic tree to ensure that distortions of the tissue did not introduce errors. For the axon terminals, we also calculated the volume and surface area of the 3D convex hull (excluding the dendrites, cell body, and axon).

2.9 | Sholl and branch order analysis of the axon terminal arbors

To perform Sholl analysis (Sholl, 1953) of the bipolar cell arborizations, we considered that the interesting target for the analysis would be the axon terminal system, excluding the axon shaft itself. To achieve this, we positioned the center point of the Sholl spheres at the origin of the axon terminal system (i.e., the end of the axon shaft). To implement this in Neurolucida 360, we modified the digital reconstruction by detaching the axon terminal from the axon shaft, with the point of detachment set to the first branch point where the axon shaft divided into (at least) two daughter branches, if at least two of three criteria were fulfilled: (1) the daughter branches had similar diameters; (2) the daughter branches had different angles of projection than the parent axon shaft; and (3) each of the daughter branches displayed at least three nodes. Finally, a small circular contour was positioned just distal to the point of detachment. This served as the center point of the Sholl spheres and ensured that the Sholl analysis was performed only for the branches of the axon terminal. The Sholl analysis was performed in 3D by a set of nested, concentric spheres with a starting radius of 1 μm and an increment of 1 μm. For branch order analysis of cone bipolar cells, we used the "central shaft" branch ordering scheme (Neurolucida Explorer). The end of the central shaft corresponded to the point of detachment used for the Sholl analysis (see above).

2.10 | Analysis of axon terminal stratification in the IPL

To calculate the axon terminal stratification profiles of the different types of cone bipolar cells, we applied a modified version of the procedures used by Helmstaedter et al. (2013) and Greene et al. (2016). The stratification profile was defined as the density of surface area vs. depth in the IPL. The borders between the IPL and INL, and between the IPL and GCL, were defined as IPL relative depths 0 and 1, respectively. The IPL was divided into 100 equally sized bins, with borders parallel to the IPL–INL and IPL–GCL borders, and process surface area was assigned to each bin. To exclude the shafts (trunks) of the axonal arbors, the analysis restricted the domain of the stratification profile to the branches of the axon terminal (as defined above), with all other bin values set to zero. Each stratification profile was normalized like a probability density function, such that the profile area integrated to unity. Percentiles were defined for a stratification profile in the same way as for a probability density function such that the interval from the *n*th percentile depth to the 0th percentile depth contains *n* percent of the area of the stratification profile (cf. Greene et al., 2016). The thickness of a stratification profile was defined as the difference between the 85th and 15th percentile depths. The center location of the stratification profile was defined as the 50th percentile depth.

2.11 | Statistical analysis and data presentation

Data are presented as mean ± SD (n = number of cells, processes or varicosities). Statistical analyses with comparisons between groups were performed with Prism (GraphPad software; RRID: SCR_002798) using Student's two-tailed t test (unpaired). Differences were considered statistically significant at the $p < .05$ level.

3 | RESULTS

3.1 | Visual targeting and identification of bipolar cells in retinal slices

In the INL, the cell bodies of bipolar cells are positioned roughly in the most distal two-thirds, with the cell bodies of amacrine cells positioned in the proximal third (Cajal, 1893). Among the bipolar cells, there is a preference for the cell bodies of rod bipolar cells to be located in the most distal region and those of cone bipolar cells to be located in the midregion of the INL (Cajal, 1893; Greferath et al., 1990). However, apart from using the location of a bipolar cell-like soma in the most distal part of the INL as a sufficient, but not necessary criterion for targeting rod bipolar cells, we found that soma position (i.e., depth in the INL) could not be used as a reliable criterion to target specific types of bipolar cells (cf. Cohen & Sterling, 1990). After establishing the whole-cell recording configuration, and switching the optical pathway from IR-DGC videomicroscopy to MPE fluorescence microscopy, we were able to verify the morphology of the recorded cell as either a cone bipolar cell or a rod bipolar cell and to acquire a complete image stack (Figure 2a–c; rightmost columns). The forward-scattered IR laser light enabled simultaneous acquisition of IR-LSGC images of the retinal slice (Figure 2a–c; leftmost column). On-line overlaying of the fluorescence and IR-LSGC images (in perfect register with each other) allowed us to identify the location (width, thickness, and stratification level) of the axon terminal of the cell within the IPL (Figure 3a). In total, 39 bipolar cells were selected for quantitative digital reconstruction and morphometric analysis.

3.2 | Workflow for morphological reconstruction of bipolar cells

Following deconvolution and spatial alignment (to correct for drift and small movements), an accurate digital reconstruction was generated for each cell by manually tracing the fluorescent processes through the image stack (see Materials and Methods). The workflow for such reconstruction is illustrated in Figure 3, with maximum intensity projections of the fluorescence image stack, before (Figure 3a) and after (Figure 3b) deconvolution and alignment, overlaid on a single, representative slice of the IR-LSGC channel image stack. A corresponding overlay of the final digital reconstruction is illustrated in Figure 3c. For enhanced visualization of finer details of the dendritic and axonal arbors, we used shape plots (two-dimensional [2D] projections; Figure 3d) or 3D visualizations (Figure 3e).

3.3 | Qualitative morphological characteristics of bipolar cells

Despite morphological variability, bipolar cells display a set of common characteristics that together contribute to defining them as a major cell class in the retina (Figure 3). First, bipolar cells generally have a medium size soma located in the distal two-thirds of the INL. Second, they have a dendritic tree (tuft) that arises from one or more processes at the distal pole of the soma and displays terminal branches ramifying in the OPL. Third, they have a single long axon that arises from the proximal pole of the soma and courses through the INL before it terminates at a specific level of the IPL and branches laterally into an elaborate axon terminal with beadlike swellings or varicosities (Figure 4). The portion of the axon between the cell body and the axon terminal will be referred to as the axon shaft. The bipolar cell axon shaft is equivalent to "axis cylinder" or "vitreal fiber" and the terminal ramifications are equivalent to the "teledendrons," as defined and used by Polyak (1941). Many of the small branchlets in the axon terminal assume a horizontal course.

The level at which the axon terminal stratification takes place in the IPL is an important defining characteristic and of fundamental importance for classifying the different types of cone bipolar cells (for rat, see Euler & Wässle, 1995). Two examples of cone bipolar cells stratifying at different levels are illustrated in Figure 4a,b. In contrast, the axon terminals of rod bipolar cells correspond to a smaller number of

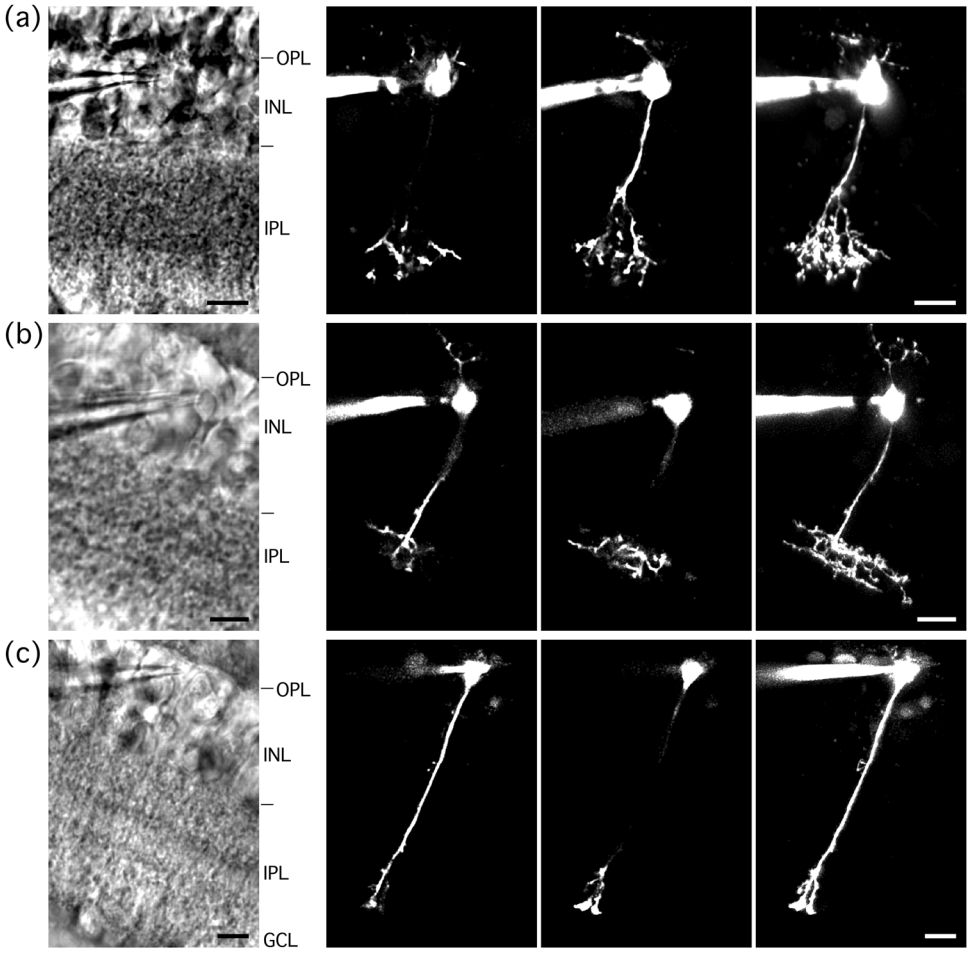

FIGURE 2 Visual targeting and multiphoton excitation (MPE) microscopy with live imaging of dye-filled bipolar cells in retinal slices. (a) Left panel: Image of retinal slice acquired with infrared (IR) laser scanning gradient contrast (IR-LSGC) microscopy. The tip of the recording pipette is located at cell body of an OFF-cone bipolar cell. Here, and in (b) and (c), the retinal layers are indicated by abbreviations (OPL, outer plexiform layer; INL, inner nuclear layer; IPL, inner plexiform layer; GCL, ganglion cell layer). Two middle panels: Individual image slices acquired with MPE microscopy after filling the OFF-cone bipolar cell with the fluorescent dye Alexa Fluor 594. Here, and in (b) and (c), each image slice is the average of two individual frames acquired at the same focal plane. Here and later, the brightly fluorescent recording pipette can be seen on the left side of the cell body. Right panel: Maximum intensity projection (MIP) of complete image stack (155 image slices, separated by 0.4 μm). Scale bar, 10 μm. (b) Left panel: IR-LSGC image of retinal slice with pipette tip at cell body of an ON-cone bipolar cell. Two middle panels: Individual MPE microscopy slices after filling ON-cone bipolar cell with Alexa Fluor 594. Right panel: MIP of complete image stack (162 image slices, separated by 0.4 μm). Scale bar, 10 μm. (c) Left panel: IR-LSGC image of retinal slice with pipette tip at cell body of a rod bipolar cell. Two middle panels: Individual MPE microscopy slices after filling rod bipolar cell with Alexa Fluor 594. Right panel: MIP of complete image stack (72 image slices, separated by 0.4 μm). Scale bar, 10 μm

considerably larger varicosities located in the proximal part of the IPL (Figure 4c; Euler & Wässle, 1995; Greferath et al., 1990).

Following Cajal (1893), the IPL of mammalian retinas is divided into five strata. In contrast to Cajal, however, who considered the strata to be of unequal thickness, it is customary to divide the IPL arbitrarily into five equally thick strata designated S1–S5 (from the most distal to the most proximal part of the IPL; Figure 4). Collectively, S1 and S2 are referred to as sublamina *a* and S3–S5 are referred to as sublamina *b* (Figure 4). Based on the morphology of their contacts with cone photoreceptors (invaginating vs. flat), it was postulated that cone bipolar cells (in cat retina) with axon terminals stratifying in sublamina *a* and *b* correspond functionally to OFF- and ON-bipolar cells, respectively (Famiglietti & Kolb, 1976; Kolb, 1979). Several years later, it was demonstrated that rat cone bipolar cells with axon terminals ending in sublamina *a* or *b* display responses to agonists of ionotropic non-NMDA-type glutamate receptors consistent with OFF- and ON-type visual response polarities, respectively (Hartveit, 1997; see also Euler et al. (1996) for similar experiments with an agonist of the metabotropic glutamate receptor mGluR6). For the examples of cone bipolar cells illustrated in Figure 4, one has an axon terminal that stratifies in S1 and S2, corresponding to the pattern associated with OFF-cone bipolar cells (Figure 4a). The cell illustrated in Figure 4b has an axon terminal that stratifies in the proximal part of S3 and the distal part of S4, corresponding to the pattern associated with ON-cone

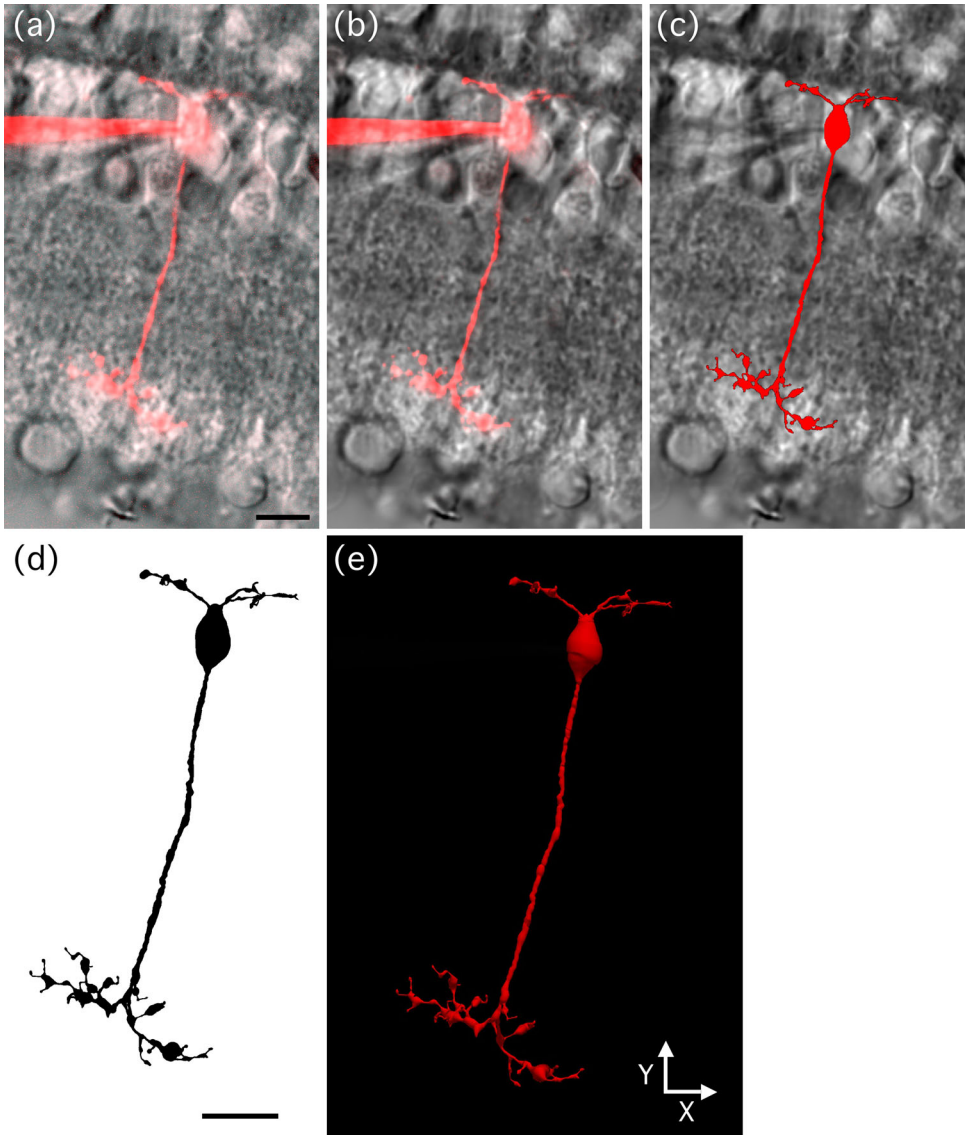

FIGURE 3 Workflow for MPE microscopic imaging and quantitative morphological reconstruction of bipolar cells. (a) MIP of raw image stack of an ON-cone bipolar cell filled with Alexa Fluor 594 during whole-cell recording (dye-filled pipette attached to the cell body) overlaid on image of retinal slice acquired with IR-LSGC microscopy. Scale bar, 10 μm (a–c). (b) Same as in (a), but after deconvolution. (c) Shape plot generated by digital morphological reconstruction of cell in (a) and (b). Brightness and contrast of background image of retina had to be readjusted for composite images (a–c). (d) Shape plot of reconstructed cell showing details of dendritic and axonal arborizations. Scale bar, 10 μm. (e) Three-dimensional (3D) view of morphological reconstruction. *X* and *Y* axes indicate spatial coordinates defined during MPE microscopic imaging, with the *Z* axis pointing toward the viewer

bipolar cells. For the classification of cone bipolar cells in our material, we used the morphological criteria based on the level of axon terminal stratification first developed by Euler and Wässle (1995; see also Hartveit, 1997). Based on these criteria, the cell in Figure 4a corresponds to a cone bipolar cell type 2 and the cell in Figure 4b corresponds to a cone bipolar cell type 6. The rod bipolar cell illustrated in Figure 4c has a distinctive appearance compared to the cone bipolar cells, with relatively short dendritic processes, and an axon with only minor side branches (in S3 and S4) before dividing into a limited number of shorter branches that end in large, varicose terminals (in S5).

The shape plots (corresponding to projections in the XY plane) of all 39 bipolar cells reconstructed in this study are displayed in Figure 5, after appropriate rotation around the *Z* and *X* axes (see Materials and Methods). Of these cells, 25 were classified as cone bipolar cells (Figure 5a–g) and 14 were classified as rod bipolar cells (Figure 5h). Of the cone bipolar cells, 10 were classified as OFF-cone bipolar cells and 15 were classified as ON-cone bipolar cells. According to the scheme proposed for cone bipolar cells in rat retina (Euler & Wässle, 1995), our material included type 2 (CBC2; $n = 2$), type 3 (CBC3; $n = 6$), type 4 (CBC4; $n = 2$), type 5 (CBC5; $n = 6$), type 6 (CBC6; $n = 6$), type 7 (CBC7; $n = 2$), and type 8 (CBC8; $n = 1$) cone bipolar cells. Of these, types 2–4 are considered to be OFF-cone bipolar cells, whereas types 5–8 are considered to be ON-cone bipolar cells (Hartveit, 1997; see also Ivanova & Müller, 2006). Unfortunately, our material did not

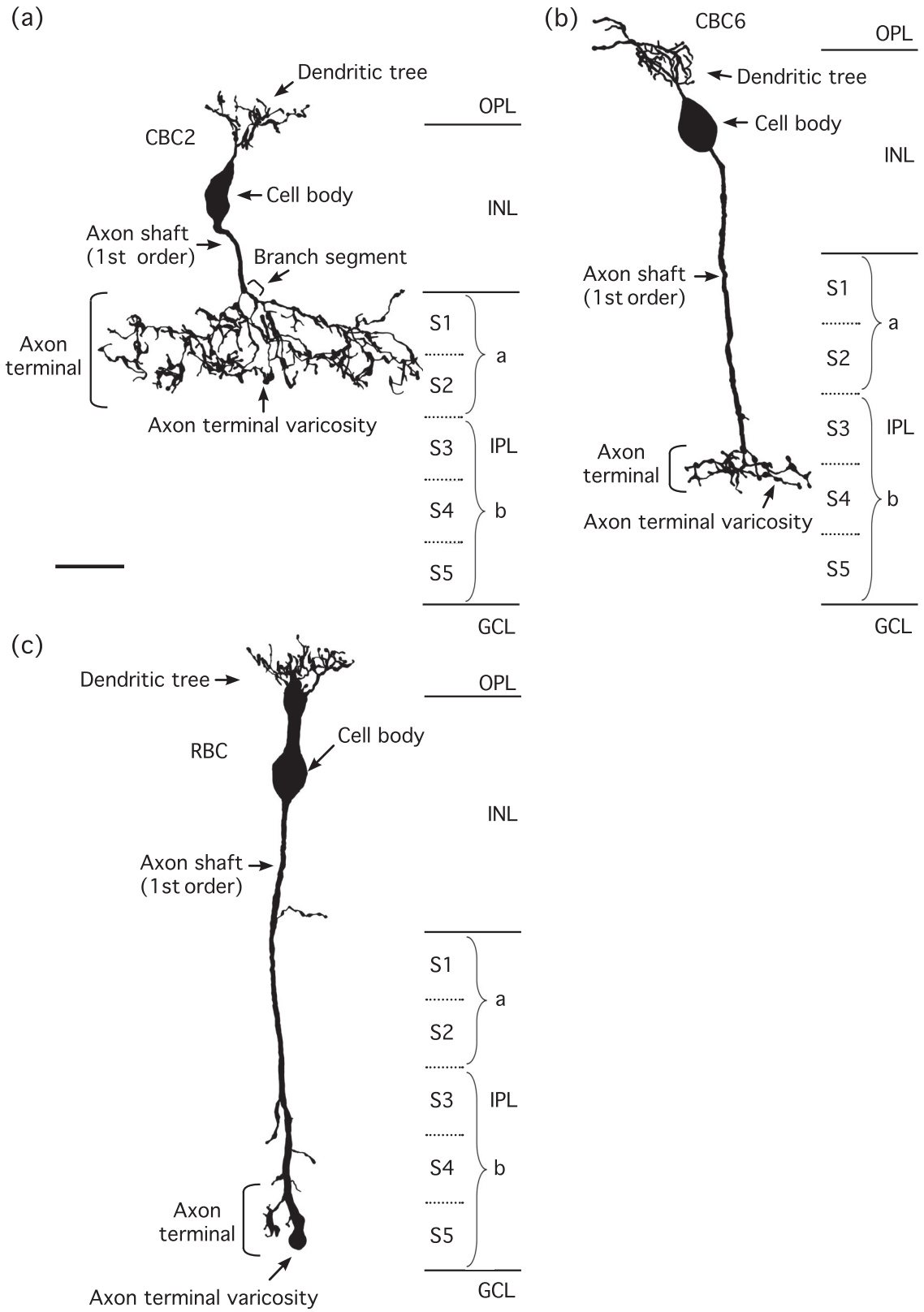

FIGURE 4 Shape plots of morphologically reconstructed cone and rod bipolar cells and nomenclature used to describe dendritic and axonal branching and branch ordering. (a) Type 2 OFF-cone bipolar cell (CBC2). Cellular morphology with shape of and relationships between cell body, dendrites, axon shaft, and axon terminal. "Branch segment" illustrates the definition of segment between two points of arborization. Axon shaft refers to the length of axon from origin at the cell body to the beginning of the axon terminal. Notice varicosities in the axon terminal. The borders between retinal layers and strata are indicated at right. The IPL has been divided into five equally thick strata (stratum 1 [S1]–S5), with S1–S2 corresponding to sublamina *a* and S3–S5 corresponding to sublamina *b*. Scale bar, 10 μm (a–c). (b) Type 6 ON-cone bipolar cell (CBC6), details as in (a). (c) Rod bipolar cell (RBC), details as in (a)

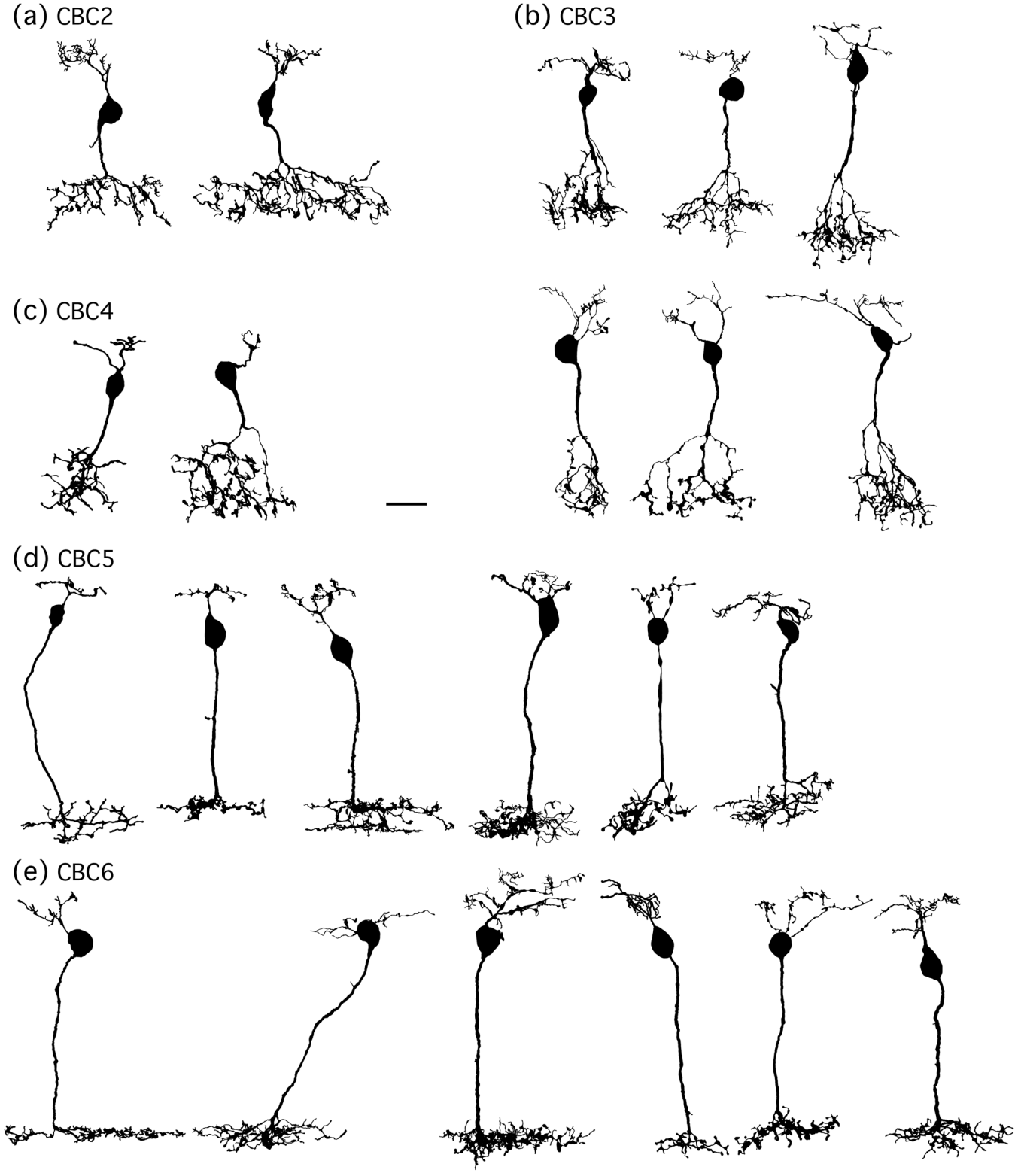

FIGURE 5 Shape plots of all morphologically reconstructed cone and rod bipolar cells ($n = 39$). (a–c) OFF-cone bipolar cells (CBC2–CBC4). (d–g) ON-cone bipolar cells (CBC5–CBC8). (h) Rod bipolar cells (RBCs). Cells were filled with Alexa Fluor 594 by whole-cell recording in retinal slices, imaged with MPE microscopy, and morphologically reconstructed. Notice common morphological properties as well as considerable heterogeneity between cell types. Some cells have been rotated in the XY plane to orient the long axis vertically. Scale bars, 10 μm

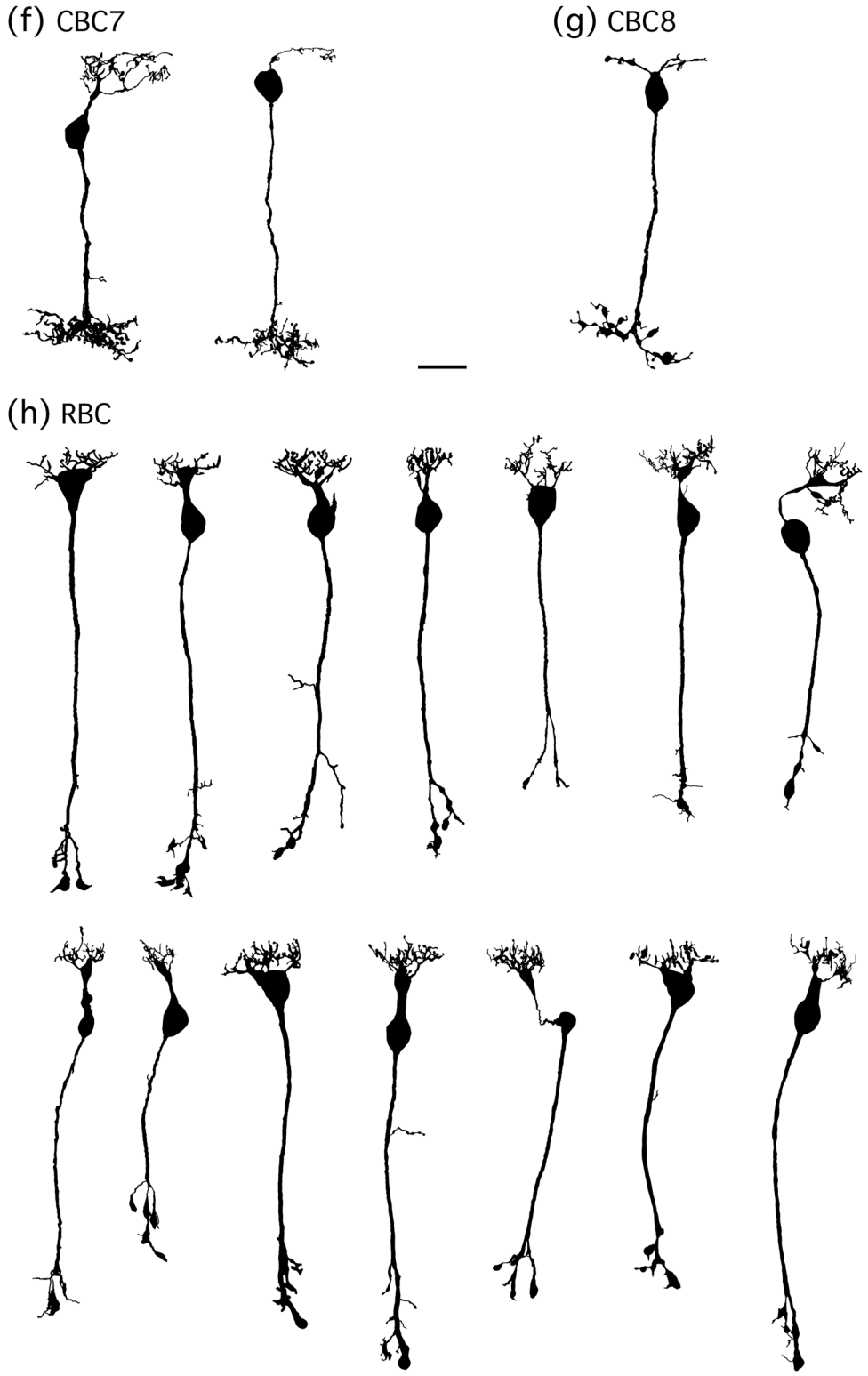

FIGURE 5 Continued

include cone bipolar cells corresponding to type 1 and type 9, most likely because these cells are relatively rare (Euler & Wässle, 1995; Hartveit, 1997; Ivanova & Müller, 2006).

Whereas the individual shape plots for the reconstructed bipolar cells (Figures 4 and 5) provide some qualitative insight into the complexity of the branching patterns of both the dendrites and the axon terminals, the high density of and considerable overlap among the processes when visualized in 2D shape plots make it difficult to appreciate the extent of branching and the number of individual processes. To more readily observe and inspect the branching patterns, especially

of the axon terminals, we generated dendrograms for all the reconstructed cells. These display the relative path lengths, branch segments, and nodes in 2D, but without any overlap. As an example of the considerable complexity of branching that can be observed for these cells, we have illustrated examples of dendrograms for both an OFF-cone (Figure 6a) and an ON-cone bipolar cell (Figure 6b), and for comparison also for a rod bipolar cell (Figure 6c).

3.4 | Distribution of axon terminals across the IPL

Because the classification of cone bipolar cells into different types relies heavily on the stratification level of their axon terminals, we performed a detailed analysis of the distribution of process length, number of varicosities, process surface area, number of endings, and number of nodes as a function of location across the depth of the IPL. For each cell, the distal and proximal borders of the IPL were determined by eye on a representative slice of the IR-LSGC image stack acquired in parallel with the fluorescence image stack. When necessary, the neuronal reconstruction and the IR-LSGC stack were rotated such that the plane of the axon terminal was horizontal (and the long axis of the axon typically vertical; see Materials and Methods). For the quantitative analysis, the depth of the IPL was defined by assigning the borders to the INL and GCL as relative depths 0 and 1, respectively (Figure 7). The thickness of the IPL was then divided into 100 equally thick strata (corresponding to bins in a histogram) that were projected onto the digital reconstructions and used to estimate the distributions. The axon shaft itself was excluded from analysis. The average stratification properties differed markedly between the different types of cone bipolar cells, with little difference between the parameters analyzed (Figure 7a–e).

To facilitate quantitative comparisons between the different types of cone bipolar cells, we calculated probability density functions for the distribution of surface area of the axon terminal processes, with normalization of the cumulative stratification profiles such that the profile density between 0 and 1 integrated to unity (Greene et al., 2016; Helmstaedter et al., 2013). We then calculated specific percentiles for the stratification profiles (see Materials and Methods) and defined the vertical thickness of each stratification profile as the difference between the 85th and 15th percentile depths. The probability density functions for process surface area of the different types of cone bipolar cells are displayed in Figure 7f and the vertical thickness profiles (relative to the depth of the IPL) are displayed in Figure 7g (see Table 1 for numerical data). The probability density functions in Figure 7f clearly demonstrate the difference between and variability within the different types of cone bipolar cells, both with respect to location across the depth of the IPL and the thickness of the distribution. From Figure 7f, it can be seen for CBC5 that three cells display a tendency toward a bistratified distribution, apparent as a segment with reduced slope between ~0.6 and ~0.8 relative density (located at 50–60% relative IPL depth). If this reflects the potential division of cells classified as CBC5 into two (or more) different types, it may be of importance that these three cells stratify at more proximal levels of the IPL than the other three CBC5 cells in our material. The thickness profiles (85th–15th percentiles) illustrated in Figure 7g suggest that despite overlap between the different types, quantitative morphological reconstruction based on MPE microscopy can provide adequate data for robust classification of individual cells.

TABLE 1 Numerical data for the stratification profiles of axon terminals for different types of cone bipolar cells

Cell type	15th percentile	50th percentile	85th percentile
CBC2	4.27	12.5	20.4
CBC3	18.5	30.0	36.9
CBC4	7.37	21.0	30.3
CBC5	43.4	47.6	53.7
CBC6	53.3	56.6	60.3
CBC7	56.8	60.9	65.5
CBC8	67.9	73.6	82.6

Note: The borders between the IPL and INL, and between the IPL and GCL, were defined as IPL relative depths 0 and 1, respectively. Percentiles were defined for a stratification profile in the same way as for a probability density function such that the interval from the *n*th percentile depth to the 0th percentile depth contains *n* percent of the area of the stratification profile (cf. Greene et al., 2016). The thickness of a stratification profile was defined as the difference between the 85th and 15th percentile depths. The center location of the stratification profile was defined as the 50th percentile depth. For additional details, see Materials and Methods.

3.5 | Quantitative morphological characteristics of bipolar cells

A qualitative description of the morphological properties of bipolar cells is fully adequate to distinguish between rod and cone bipolar cells and to distinguish between types of cone bipolar cells where the axon terminals display markedly different stratification levels, for example, at opposite ends of the IPL. However, for some types of cone bipolar cells, it can be more challenging to assign individual cells to one or the other type with similar axon terminal stratification. For example, it can be difficult to classify a specific cell as a CBC5 or CBC6, or as a CBC3 or CBC4. Two developments have increased the complexity of classification. First, physiological and immunocytochemical investigations suggest that some morphologically defined types of cone bipolar cells in reality encompass more than one type. The redefined cell types may, for example, have very similar morphological properties (i.e., level of stratification in the IPL), but may be distinguished by a difference in physiological properties, for example, expression of specific types of ion channels (Cui & Pan, 2008; Fyk-Kolodziej & Pourcho, 2007; Ivanova & Müller, 2006; Vielma & Schmachtenberg, 2016). In some cases, the purported morphological differences are subtle and have not been subjected to a detailed morphological analysis based on high-resolution imaging (e.g., Ivanova & Müller, 2006). Second, separation of cell types based on subtle differences in the level of stratification in the IPL has resulted from ultrastructural connectomics data from the mouse retina, where complete skeleton reconstructions of all cells

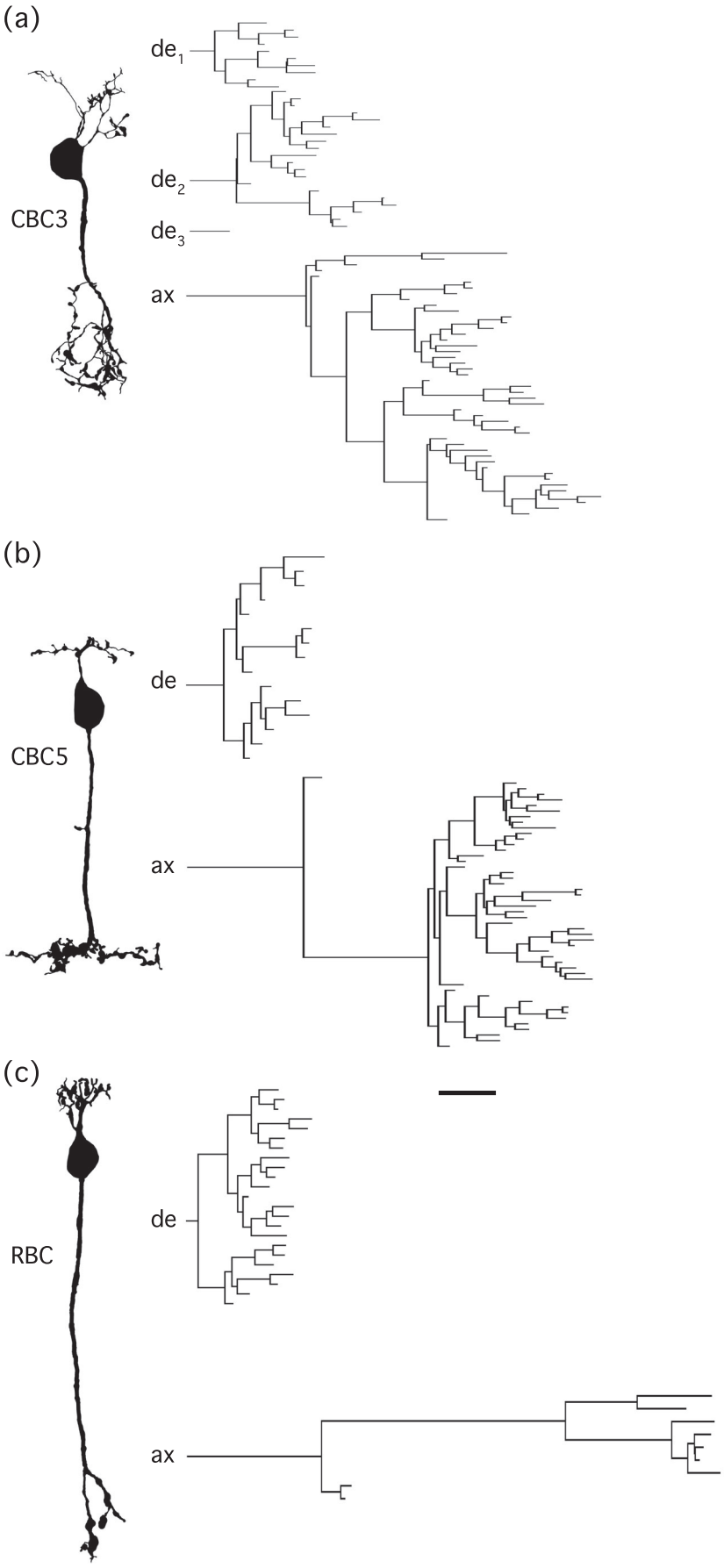

FIGURE 6 Shape plots and dendrograms (a–c) for morphologically reconstructed cone and rod bipolar cells. (a) Type 3 OFF-cone bipolar cell (CBC3). Here, and in (b) and (c), dendrograms are illustrated separately for dendritic (de) and axonal (ax) trees emanating independently from the cell body. Trees of the same kind sprouting independently from the cell body indicated by subscripts. The length of each horizontal line in the dendrograms corresponds to the path length of the corresponding branch segment. (b) Type 5 ON-cone bipolar cell (CBC5). (c) Rod bipolar cell (RBC). Scale bar, 10 μm (a–c)

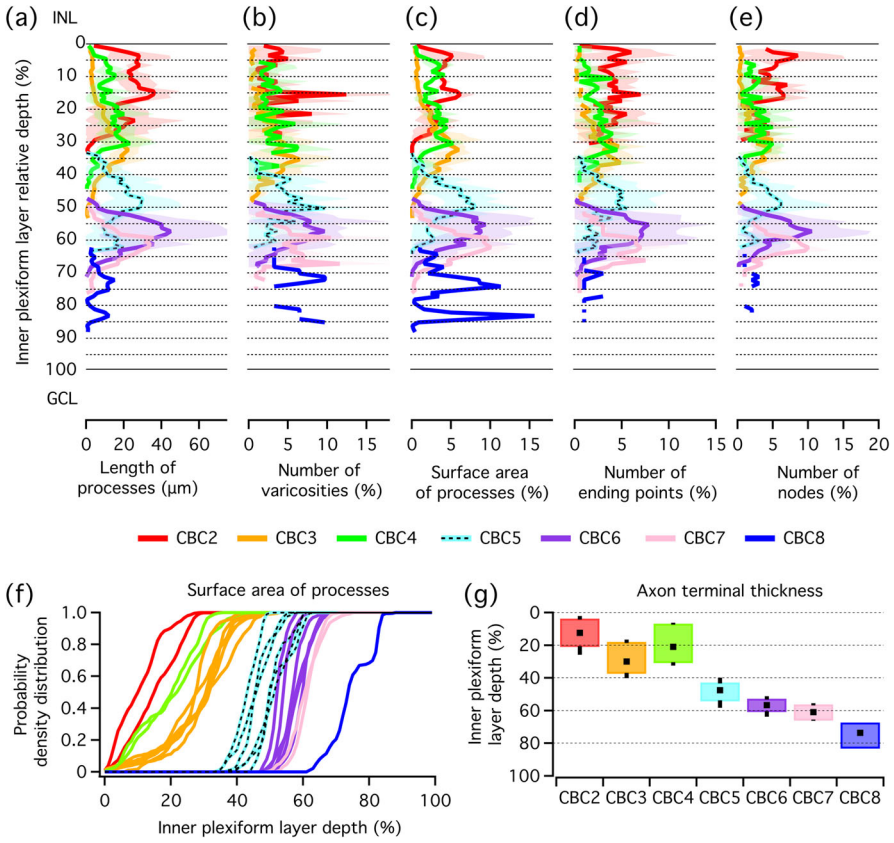

FIGURE 7 Axon terminal parameters as a function of location in the IPL for the different types of cone bipolar cells (CBC2–CBC8; color code in inset between panels). Here and later, location is indicated as relative depth, with the IPL divided into 100 equally sized bins, with 0% corresponding to the border between the IPL and INL and 100% corresponding to the border between the IPL and GCL. For each cell, only the processes defined as belonging to the axon terminal were included in the analysis. (a) Length of processes as a function of relative depth. Here and in (b–e), data are plotted as mean (continuous line in saturated color) ± SD (shaded region in desatured color). (b) Number of varicosities (relative). (c) Surface area of processes (relative). (d) Number of ending points (relative). (e) Number of nodes (relative). Any contribution of processes located in either the INL or GCL was ignored. (f) Distribution of surface area of axon terminal processes in the IPL, represented as the cumulative probability density distribution vs. relative depth of the IPL. Each continuous line corresponds to an individual cone bipolar cell. To exclude the shafts of the axonal arbors, the analysis restricted the domain of the stratification profile to the branches defined as belonging to the axon terminal, with all other bin values set to zero. Each stratification profile was normalized like a probability density function, such that the profile area integrated to unity. (g) Thickness of axon terminal stratification profiles (in the XY plane) for the different types of cone bipolar cells. Thickness was defined as the difference between the 85th and 15th percentile depths, with percentiles defined for a given stratification profile (probability density function as in [f]) such that the interval from the *n*th percentile depth to the 0th percentile depth contains *n* percent of the area of the stratification profile. For each cell type, the upper and lower margins of the colored box represent the average 15th and 85th percentile depths, respectively, with the black vertical lines representing the SD value. The black square inside each box represents the average of the center location of the stratification profile, corresponding to the 50th percentile depth

within a tissue volume enabled combined analysis of stratification and tiling properties. Specifically, observation of tiling violations enabled reclassification of cone bipolar cells as different types, despite very similar stratification (Greene et al., 2016; Helmstaedter et al., 2013). Importantly, such decisions depended on the subjective judgment of human observers.

Because of the challenge of classifying individual cone bipolar cells in physiological experiments with intracellular recording, we wondered if quantitative analysis of other morphological properties in addition to the axon terminal stratification might facilitate classification. As there is a paucity of relevant quantitative morphological data at the light microscopic level, we used our reconstructions to obtain data for neuronal arborization, including branching pattern, process lengths and diameters, surface area, and number and distribution of axon terminal varicosities. The results of our analysis of a series of geometric and topological parameters of neuronal morphology for all bipolar cells in this study are summarized in Table 2.

There was considerable overlap between the different types of OFF- and ON-cone bipolar cells for almost all morphological parameters analyzed (Table 2). If future investigations indicate that currently recognized types of cone bipolar cells should be split into two (or more) types (see Discussion), it is in principle possible that some of the overlap will be reduced, but given the extensive overlap observed for all types, this seems relatively unlikely. Despite the considerable variability both between and within specific types of cone bipolar cells, it seems that the arborizations of their axon terminals follow the same, or at least very similar, underlying geometric rules. Rod bipolar cells display qualitatively different morphology from the majority of cone bipolar

TABLE 2 Morphological properties of reconstructed bipolar cells

Parameter	CBC2 ($n = 2$) Mean ± SD (range)	CBC3 ($n = 6$) Mean ± SD (range)	CBC4 ($n = 2$) Mean ± SD (range)	CBC5 ($n = 6$) Mean ± SD (range)	CBC6 ($n = 6$) Mean ± SD (range)	CBC7 ($n = 2$) Mean ± SD (range)	CBC8 ($n = 1$) Mean	RBC ($n = 14$) Mean ± SD (range)
Total cell surface area (μm^2)	998 ± 222 (841–1155)	754 ± 111 (645–917)	836 ± 166 (718–953)	881 ± 194 (642–1128)	1017 ± 359 (637–1670)	845 ± 351 (597–1094)	598	601 ± 120 (428–854)
Total cell volume (μm^3)	153 ± 4 (150–156)	156 ± 18 (140–182)	178 ± 40 (150–207)	184 ± 56 (102–257)	212 ± 54 (165–315)	183 ± 36 (158–209)	171	185 ± 44 (98–250)
Soma surface area (μm^2)	76 ± 17 (64–88)	92 ± 19 (72–120)	91 ± 26 (72–109)	91 ± 28 (51–130)	104 ± 11 (90–121)	96 ± 10 (89–103)	89	104 ± 25 (40–137)
Soma volume (μm^3)	59 ± 27 (40–79)	82 ± 28 (52–124)	77 ± 31 (56–99)	79 ± 33 (32–122)	97 ± 14 (81–119)	87 ± 18.3 (74–100)	72	95 ± 32 (23–132)
Soma projection (XY) area (μm^2)	21.2 ± 2.7 (19.2–23.1)	25.5 ± 4.7 (21.0–32.7)	25.7 ± 7.4 (20.5–31.0)	25.8 ± 8.1 (14.4–37.6)	28.6 ± 2.7 (24.21–31.5)	27.1 ± 2.0 (25.7–28.5)	26.0	29.7 ± 7.1 (11.3–40.6)
Soma projection (XY) perimeter (μm)	18.5 ± 1.2 (17.7–19.3)	19.3 ± 1.9 (17.9–22.3)	19.8 ± 3.6 (17.3–22.3)	19.6 ± 3.4 (15.0–25.3)	20.7 ± 1.6 (18.3–22.7)	20.4 ± 0.7 (19.9–20.9)	20.8	22.4 ± 4.0 (13.3–30.4)
Soma projection (XY) Feret max (μm)	7.0 ± 1.4 (6.0–8.0)	7.1 ± 0.5 (6.5–8.0)	7.8 ± 1.6 (6.7–9.0)	7.4 ± 1.5 (5.7–10.0)	7.5 ± 0.9 (6.4–8.6)	7.6 ± 0.5 (7.2–8.0)	8.5	8.6 ± 2.0 (4.9–13.1)
Soma projection (XY) Feret min (μm)	4.3 ± 1.1 (3.5–5.0)	4.9 ± 0.8 (3.8–5.7)	4.7 ± 0.7 (4.2–5.1)	4.51 ± 0.77 (3.34–5.25)	5.32 ± 0.36 (4.93–5.96)	4.89 ± 0.45 (4.57–5.20)	4.36	4.94 ± 0.90 (2.96–6.13)
Number of primary dendrites	1.50 ± 0.71 (1–2)	1.67 ± 0.82 (1–3)	1.00 ± 0.00 (1–1)	1.5 ± 0.8 (1–3)	2.0 ± 1.3 (1–4)	1.5 ± 0.7 (1–2)	2.0	2.1 ± 1.4 (1–5)
Number of endings (dendrites)	51 ± 27 (32–70)	26 ± 7 (17–37)	9 ± 5 (5–24)	22 ± 13 (9–43)	37 ± 21 (14–69)	30 ± 28 (10–50)	8	39 ± 12 (23–60)
Number of nodes (dendrites)	50 ± 25 (32–67)	24 ± 7 (15–35)	8 ± 5 (4–11)	20 ± 13 (7–42)	35 ± 21 (12–67)	29 ± 28 (9–49)	6	37 ± 12 (22–59)
Dendritic length (μm)	174 ± 50 (138–209)	149 ± 39 (92–200)	61 ± 32 (38–84)	120 ± 41 (84–172)	202 ± 111 (97–395)	161 ± 136 (66–257)	75	175 ± 59 (97–273)
Axon shaft diameter** (μm)	0.78 ± 0.11 (0.70–0.86)	0.72 ± 0.07 (0.62–0.83)	0.82 ± 0.03 (0.80–0.84)	0.68 ± 0.06 (0.60–0.75)	0.70 ± 0.08 (0.61–0.81)	0.67 ± 0.17 (0.55–0.79)	0.72	0.76 ± 0.10 (0.59–0.90)
Axon shaft length (μm)	16.0 ± 3.4 (13.6–18.4)	19.4 ± 6.7 (6.9–25.1)	13.4 ± 5.8 (9.3–17.5)	48 ± 12 (39–70)	53 ± 5 (44–56)	46 ± 9 (39–53)	47	56 ± 10 (36 – 75)
Axon terminal surface area (μm^2)	726 ± 274 (532–920)	491 ± 107 (339–642)	617 ± 216 (464–770)	545 ± 150 (355–748)	596 ± 272 (208–1051)	505 ± 211 (356–655)	311	131 ± 42 (72–209)
Axon terminal volume (μm^3)	71 ± 29 (51–92)	55 ± 14 (38–71)	80 ± 22 (65–96)	70 ± 21 (40–94)	75 ± 37 (25–132)	66 ± 34 (42–90)	68	26.7 ± 9.7 (8.2- 46.7)
Axon terminal total length (μm)	680 ± 250 (503–856)	424 ± 82 (315–533)	445 ± 215 (293–598)	413 ± 149 (251–607)	464 ± 221 (158–833)	370 ± 102 (297–442)	158	69 ± 23 (37–116)
Axon terminal average branch segment path length (μm)*	2.82 ± 0.65 (2.40–3.28)	3.03 ± 0.35 (2.50–3.41)	2.78 ± 0.21 (2.63–2.93)	2.89 ± 0.41 (2.22–3.32)	2.99 ± 0.74 (2.16–3.92)	2.23 ± 0.42 (1.93–2.53)	3.43	5.0 ± 2.7 (2.3–12.3)
Maximum branch order (central shaft ordering)	22.5 ± 0.7 (22–23)	17.2 ± 3.7 (12–23)	20.0 ± 1.4 (19–21)	16.5 ± 3.4 (12–21)	18.8 ± 5.8 (13–28)	21.0 ± 2.8 (19–23)	9	3.7 ± 1.1 (2–6)
Number of nodes (axon shaft)	1.5 ± 0.7 (1–2)	1.2 ± 1.1 (0–3)	1.0 ± 0.0 (1–1)	2.00 ± 0.89 (1–3)	2.33 ± 0.82 (1–3)	5.00 ± 0.00 (5–5)	1	2.3 ± 1.4 (1–6)
Number of endings (axon shaft)	0.50 ± 0.71 (0–1)	0.33 ± 0.89 (0–2)	0 n.a.	1.00 ± 0.89 (0–2)	1.33 ± 0.82 (0–2)	4.00 ± 0.00 (4–4)	0	1.3 ± 1.6 (0–6)

(Continues)

TABLE 2 (Continued)

Parameter	CBC2 ($n = 2$) Mean ± SD (range)	CBC3 ($n = 6$) Mean ± SD (range)	CBC4 ($n = 2$) Mean ± SD (range)	CBC5 ($n = 6$) Mean ± SD (range)	CBC6 ($n = 6$) Mean ± SD (range)	CBC7 ($n = 2$) Mean ± SD (range)	CBC8 ($n = 1$) Mean	RBC ($n = 14$) Mean ± SD (range)
Number of nodes (axon terminal)	118 ± 17 (106–130)	71 ± 19 (46–97)	80 ± 43 (49–111)	74 ± 36 (42–135)	87 ± 47 (22–155)	83 ± 8 (77–88)	22	7.4 ± 3.6 (4–17)
Number of endings (axon terminal)	119 ± 14 (109–129)	73 ± 19 (47–99)	82 ± 45 (50–114)	76 ± 36 (45–137)	88 ± 46 (25–156)	83 ± 7 (78–88)	24	9.1 ± 3.5 (6–18)
Average partition asymmetry (axon terminal)*	0.644 ± 0.014 (0.634–0.654)	0.600 ± 0.044 (0.551–0.668)	0.645 ± 0.031 (0.624–0.667)	0.567 ± 0.051 (0.528–0.658)	0.620 ± 0.057 (0.566–0.725)	0.605 ± 0.078 (0.550–0.660)	0.511	0.55 ± 0.18 (0.80–0.10)
Number of varicosities	55 ± 41 (26–84)	55 ± 11 (46–74)	49 ± 15 (38–59)	55 ± 23 (29–88)	66 ± 38 (25–130)	50 ± 8 (44–55)	31	6.1 ± 2.5 (2–11)
Average diameter of varicosities (μm)	0.570 ± 0.014 (0.56–0.58)	0.538 ± 0.032 (0.49–0.58)	0.630 ± 0.028 (0.61–0.65)	0.59 ± 0.07 (0.51–0.70)	0.56 ± 0.09 (0.45–0.71)	0.57 ± 0.15 (0.46–0.67)	0.68	1.07 ± 0.20 (0.85–1.52)
2D convex hull area (XZ), dendrites (μm^2)†	135 ± 53 (97–172)	286 ± 90 (179–389)	88 ± 107 (12–164)	224 ± 82 (107–344)	376 ± 259 (136–880)	288 ± 222 (131–445)	267	133 ± 34 (78–178)
2D convex hull perimeter (XZ), dendrites (μm)†	46 ± 12 (38–55)	64 ± 17 (46–88)	37 ± 32 (15–59)	59 ± 10 (41–70)	78 ± 20 (49–111)	68 ± 20 (54–82)	63.5	46.0 ± 6.6 (35.8–60.7)
2D convex hull Feret max (XZ), dendrites (μm)†	18 ± 6 (14–22)	28 ± 8 (20–39)	16 ± 15 (5–26)	22.2 ± 2.8 (17.0–24.5)	32.0 ± 7.7 (19.2–40.9)	23.6 ± 6.2 (16.9–29.2)	21.9	17.2 ± 3.5 (10.4–24.8)
2D convex hull Feret min (XZ), dendrites (μm)†	10.3 ± 0.8 (9.7–10.8)	14.9 ± 1.7 (12.0–17.3)	6.7 ± 3.5 (4.2–9.2)	14.4 ± 3.5 (9.2–18.6)	15.9 ± 7.6 (11.0–30.2)	12.3 ± 5.0 (8.9–18.0)	17.7	11.0 ± 2.2 (7.1–15.0)
Aspect ratio (Feret max/Feret min), dendrites†	1.65 ± 0.14 (1.55–1.74)	1.77 ± 0.55 (1.34–2.49)	1.35 ± 0.26 (1.17–1.53)	1.44 ± 0.17 (1.30–1.66)	1.48 ± 0.07 (1.38–1.55)	1.68 ± 0.04 (1.65–1.71)	1.9	1.75 ± 0.47 (1.33–2.98)
2D convex hull area (XZ), axon terminal (μm^2)†	1031 ± 764 (491–1572)	436 ± 62 (388–543)	414 ± 154 (332–523)	570 ± 163 (358–856)	778 ± 283 (329–1184)	403 ± 57 (363–444)	273	52 ± 21 (23–111)
2D convex hull perimeter (XZ), axon terminal (μm)†	121 ± 53 (83–158)	83 ± 5 (77–89)	77 ± 16 (67–88)	92 ± 12 (76–114)	107 ± 23 (70–139)	79 ± 4 (77–82)	66	28.8 ± 5.6 (20.9–43.8)
2D convex hull Feret max (XZ), axon terminal (μm)†	47 ± 23 (31–63)	32 ± 3 (28–37)	27 ± 7 (23–32)	33.6 ± 4.9 (30.2–43.3)	39.9 ± 8.2 (27.0–52.8)	30.7 ± 3.2 (28.4–32.8)	26.5	11.3 ± 2.6 (8.7–18.3)
2D convex hull Feret min (XZ), axon terminal (μm)†	28 ± 12 (20–36)	19 ± 3 (13–22)	20 ± 1 (19–21)	23.4 ± 2.7 (18.2–26.1)	27.0 ± 5.5 (17.8–34.6)	18.3 ± 2.4 (16.7–20.0)	14.8	6.7 ± 1.4 (3.8–9.4)
Aspect ratio (Feret max/Feret min), axon terminal†	1.7 ± 0.4 (1.4–2.0)	1.9 ± 0.5 (1.3–2.5)	2.0 ± 1.2 (1.2–2.9)	1.6 ± 0.3 (1.3–2.0)	2.2 ± 0.8 (1.4–3.5)	2.5 ± 1.2 (1.6–3.3)	1.2	1.63 ± 0.46 (0.69–2.49)
3D convex hull surface area, axon terminal (μm^2)	2807 ± 1729 (1584–4030)	1561 ± 199 (1279–1790)	1549 ± 533 (1172–1926)	1482 ± 402 (1047–2229)	1841 ± 591 (881–2589)	1077 ± 109 (1000–1154)	1000	300 ± 123 (117–664)
3D convex hull volume, axon terminal (μm^3)	10,024 ± 7523 (4705–15,344)	4561 ± 976 (3612–5872)	4814 ± 2209 (3253–6376)	3632 ± 1383 (2335–6083)	4073 ± 1534 (1594–6397)	2218 ± 311 (1998–2438)	1998	333 ± 220 (73–943)

(Continues)

TABLE 2 (Continued)

Parameter	CBC2 ($n = 2$) Mean ± SD (range)	CBC3 ($n = 6$) Mean ± SD (range)	CBC4 ($n = 2$) Mean ± SD (range)	CBC5 ($n = 6$) Mean ± SD (range)	CBC6 ($n = 6$) Mean ± SD (range)	CBC7 ($n = 2$) Mean ± SD (range)	CBC8 ($n = 1$) Mean	RBC ($n = 14$) Mean ± SD (range)
Ratio between dendritic and axon terminal tree 2D convex hull areas†	0.15 ± 0.06 (0.11–0.20)	0.65 ± 0.16 (0.42–0.82)	0.28 ± 0.36 (0.02–0.54)	0.39 ± 0.11 (0.30–0.60)	0.53 ± 0.30 (0.11–0.93)	0.68 ± 0.45 (0.36–1.00)	0.98	3.0 ± 1.5 (1.4–7.0)
Bifurcation angle of axon terminal (mean) (deg)*	91.3 ± 1.7 (90.1–92.5)	91.7 ± 5.4 (84.8–98.5)	95.8 ± 2.6 (94.0–97.7)	93.1 ± 4.1 (86.9–98.9)	93.0 ± 4.9 (87.6–100.7)	96.5 ± 4.2 (93.5–99.4)	85.8	74 ± 11 (61–93)
Bifurcation angle of axon terminal (standard deviation)*	34.5 ± 0.2 (34.4–34.6)	32.7 ± 2.5 (29.7–36.2)	27.9 ± 1.6 (26.7–29.1)	29.7 ± 2.9 (25.7–33.1)	33.2 ± 3.5 (28.3–38.5)	30.61 ± 2.7 (28.7–32.5)	27.7	24.4 ± 9.8 (4.3–35.8)

Note: Metrics were obtained from Neurolucida Explorer, except those marked with * (from L-measure) and † (from IGOR Pro). For some metrics where it would otherwise not be obvious, the L-measure function names are stated in parenthesis. For all metrics (except bifurcation angle), each cell contributed one data point and the averages and SDs were calculated for each cell type.

Average partition asymmetry: a measure for how much a neuronal tree deviates from a symmetrically partitioned tree where each node gives rise to two subtrees that contain an equal number of nodes, with 0 corresponding to a perfectly symmetric tree and 1 corresponding to a maximally uneven distribution of nodes, that is, a tree containing a single long process with only single branches sprouting off.

Bifurcation angle: measures the angle between the two daughter branch segments of a bifurcation (angle measured between lines connecting the start and end points of the daughter segments).

** See description of calculation of axon diameter in Materials and Methods.

n.a, not applicable.

cells and this is reflected in several morphological parameters. On average, they also have larger cell bodies than cone bipolar cells, but with considerable overlap.

3.6 | Dendritic and axon terminal fields

We analyzed the dendritic and axonal fields of all the reconstructed bipolar cells after projecting the reconstruction points of the dendritic and axonal arbors onto the XZ plane (equivalent to the retinal surface) and estimated the 2D convex hulls for both fields. Prior to generating the XZ projections, each cone bipolar cell was first rotated around the *X* and *Z* axes to ensure that the plane of the axon terminal and/or the dendritic tree was oriented approximately horizontal, that is, parallel to the XZ plane (see Materials and Methods). For rod bipolar cells, similar rotations were done, but with the goal of orienting the distal axon and the axon terminals approximately vertical in both the XY and YZ planes. After generating the 2D convex hulls for both the dendritic and axonal arborizations, we calculated the area, perimeter, Feret max, Feret min, aspect ratio (Feret max/Feret min), and the ratio between the areas of dendritic and axonal fields (Table 2). Projections of the reconstruction points together with the 2D convex hulls for both the dendritic and axon terminal fields are shown for all reconstructed cells in Figure 8 (cone bipolars) and Figure 9 (rod bipolars; note that the scaling for the rod bipolars is different from the cone bipolars).

For most cone bipolar cells (both OFF and ON), the area of the dendritic field was consistently smaller than that of the axon terminal field (Figure 10a). The smallest ratio between dendritic and axon terminal area was observed for CBC2 (0.15 ± 0.06, $n = 2$) and the largest ratio was seen for CBC7 (0.68 ± 0.45, $n = 2$) and CBC8 (0.98, $n = 1$; see Table 2 for complete data). No type of cone bipolar cell displayed a larger area for the dendritic field than for the axon terminal field (Figures 8a–g and 10a). In contrast, for rod bipolar cells, the area of the dendritic field was consistently larger than the area of the axon terminal field, with an average ratio of 3.0 ± 1.5 (range 1.4–7.0; Figures 9 and 10a,b). The dendritic field area was approximately 100–400 μm^2 for both rod and cone bipolar cells, but the axon terminal field area was several-fold larger for cone than rod bipolar cells (Figures 8–10a,b).

For the cone bipolar cells, there was a weak positive correlation between the area of the dendritic field and the area of the axon terminal field (Figure 10a). We also examined the scaling of the axon terminal and dendritic fields by plotting the process lengths vs. the corresponding areas (Figure 10c,d). For the axon terminal fields, there was an almost linear relationship between these two parameters (Figure 10c), indicating that larger axon terminal field sizes are not simply generated by a different structural organization of a more or less constant total length of processes. For the dendritic fields, a similar relationship was observed, but with larger scatter (Figure 10d).

To examine whether larger axon terminal and dendritic fields of cone bipolar cells primarily correspond to a simple scaling or rather to an increase in branching density and/or complexity, we plotted the number of axon terminal (or dendritic) segments (equal to the sum of the number of nodes and the number of endings) as a function of the axon terminal (or dendritic) field area (Figure 10e,f). For the axon

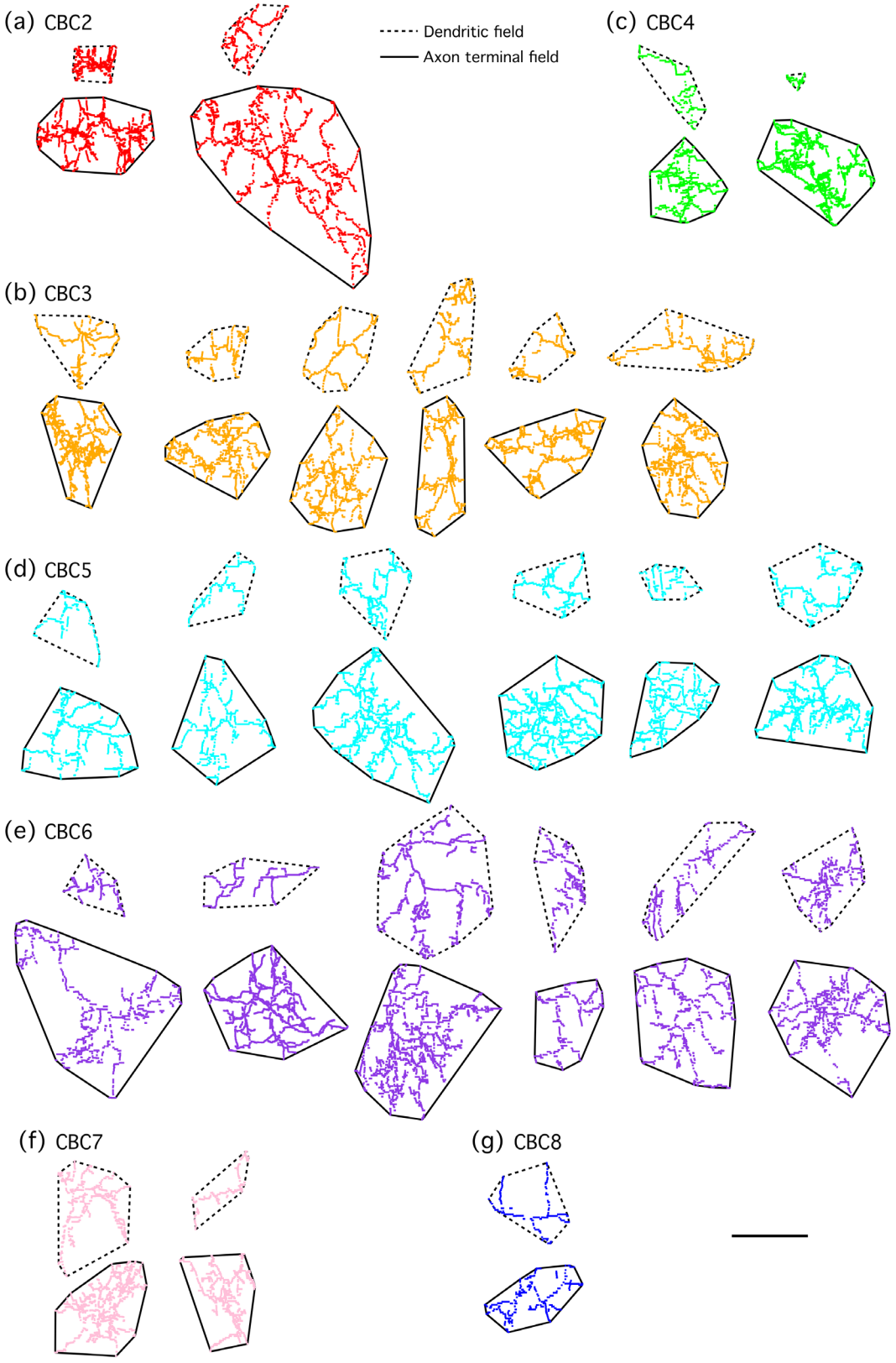

FIGURE 8 Dendritic and axon terminal fields of all morphologically reconstructed cone bipolar cells. (a–c) OFF-cone bipolar cells (CBC2–CBC4). (d–g) ON-cone bipolar cells (CBC5–CBC8). For each field (dendrite, axon terminal), each dot corresponds to a reconstruction point and all reconstruction points were projected onto the XZ plane (the plane of the retinal surface). When required, a reconstruction was first rotated around the *X* and *Z* axes such that the plane of the dendritic tree and/or axon terminal was aligned parallel to the XZ plane, maximizing the area of projection in this plane and minimizing the thickness when projected onto the XY and YZ planes. The two-dimensional (2D) convex hull for each dendritic and axon terminal field is indicated by the broken and continuous lines, respectively. Scale bars, 20 μm (a–g)

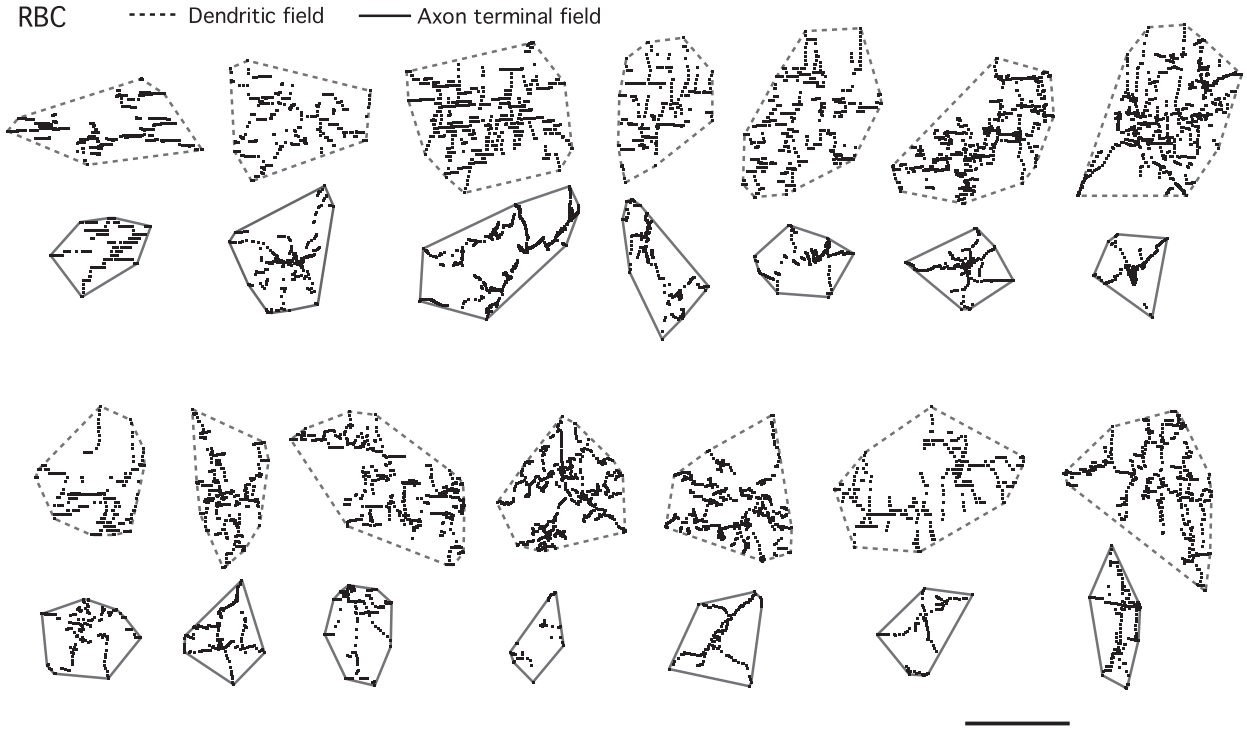

FIGURE 9 Dendritic and axon terminal fields of all morphologically reconstructed rod bipolar cells (RBCs). For each field (dendrite, axon terminal), each dot corresponds to a reconstruction point and all reconstruction points were projected onto the XZ plane (the plane of the retinal surface). When required, a reconstruction was first rotated around the *X* and *Z* axes such that the plane of the dendritic tree and/or axon terminal was aligned parallel to the XZ plane, maximizing the area of projection in this plane and minimizing the thickness when projected onto the XY and YZ planes. The 2D convex hull for each dendritic and axon terminal field is indicated by the broken and continuous lines, respectively. Scale bar, 10 μm

terminal fields, there was an almost linear relationship, suggesting that larger field sizes correspond to an increase in the branching complexity and not a simple scaling (Figure 10e). The relationship between the number of dendritic segments and field size was similar, but less pronounced, with considerable variability of the number of segments for a given dendritic field area (Figure 10f).

For rod bipolar cells, both dendritic and axon terminal fields were considerably smaller than for cone bipolar cells (Figure 10a,b). Overall, the rod bipolar cells adhered to the same relationships as the cone bipolar cells for axon terminal fields (Figure 10c,e). However, for the dendritic fields, rod bipolar cells displayed longer process lengths and a larger number of segments for a given dendritic field size (Figure 10d,f). This is likely to reflect the much higher density of rods compared to cones in rat retina (Szél & Röhlich, 1992).

3.7 | Axon terminal parameters as a function of branch order

From the shape plots (Figure 5), it is readily apparent that the axon terminals of our cone bipolar cells display a much larger extent and complexity of branching compared to earlier illustrations based on Golgi impregnation or cells filled or labeled with fluorescent dyes (e.g., Euler & Wässle, 1995; Ghosh et al., 2004; Hartveit, 1997; Hellmer et al., 2016; Ivanova & Müller, 2006; Keeley & Reese, 2010; Pignatelli & Strettoi, 2004; Vielma & Schmachtenberg, 2016). We are not aware of previous studies that have attempted to quantify and compare the extent and complexity of branching, for example, by calculating the maximum branch order and the average length of processes for each branch order. There are two generally used branch ordering schemes that can be applied to analyze axon terminal parameters as a function of branch order. In the centrifugal branch ordering scheme, each branch point leads to an increase in branch order of the daughter segments, whereas in the central shaft branch ordering scheme, the branch order of a main process (in this case, the axon shaft; Figure 4) remains constant at 1 along its length. Any smaller segments that branch off the main process are each assigned a branch order of 2. A bipolar cell axon shaft is essentially unbranched, despite the presence in some cells of short side branches ("twigs") as the axon shaft passes between its origin at the soma and its end at the beginning of the axon terminal in the IPL (Figures 4 and 5). Accordingly, applying the central shaft branch ordering is a natural choice for the analysis of cone bipolar cell axon terminals (Figure 11). Among these cells, the highest branch order was 21–23, except for CBC6 and CBC8, where it was 29 and 9, respectively (Figure 11a). The number of segments peaked between branch order 8 and 12 (Figure 11b). Importantly, for all types of cone bipolar cells, process length (Figure 11c), process surface area (Figure 11d), process volume (Figure 11e), number of nodes (Figure 11f), and number of endings (Figure 11g) were moderately skewed toward lower branch orders, with few or no consistent differences between different cell types.

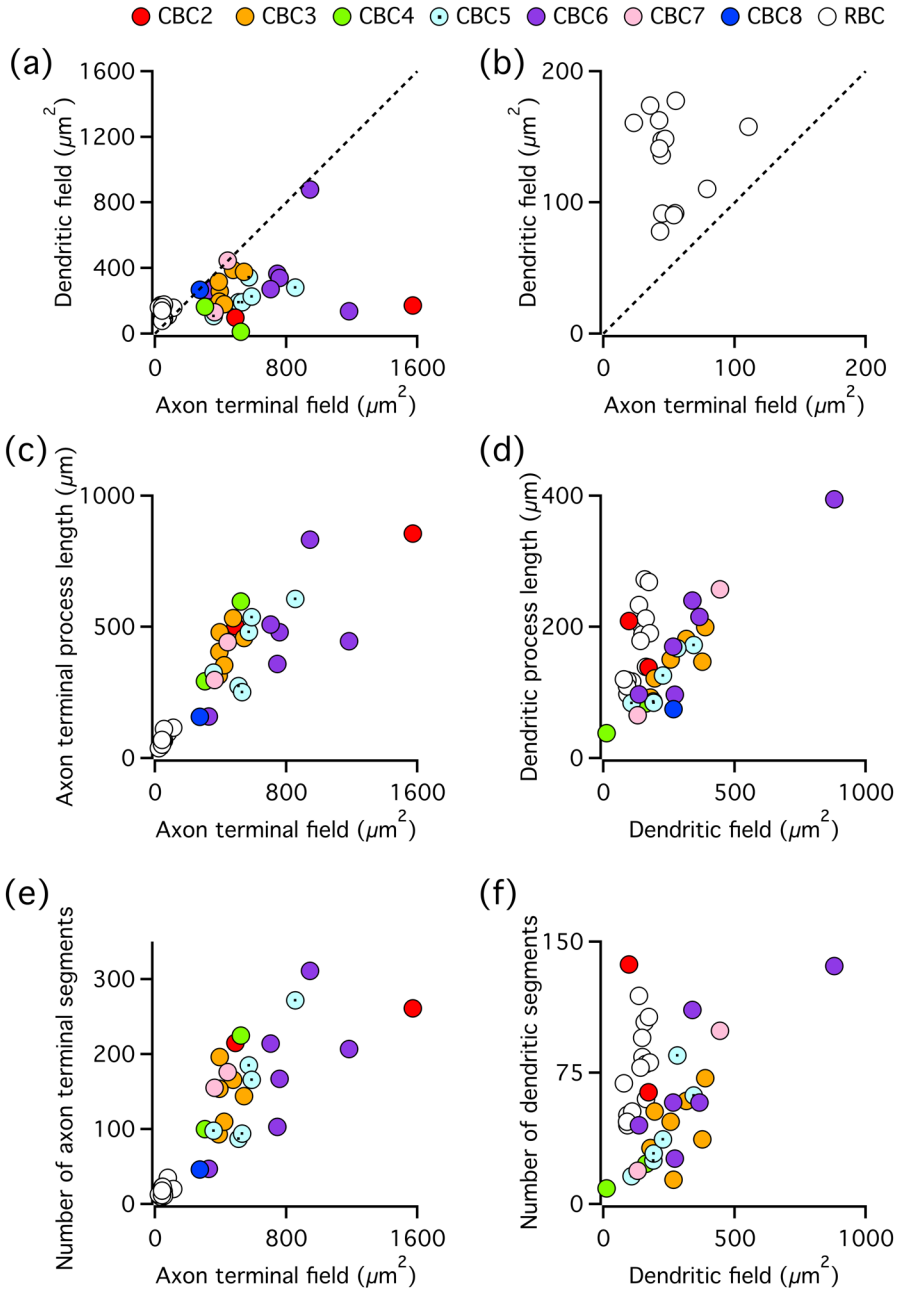

FIGURE 10 Morphological properties of cone and rod bipolar cells as a function of dendritic and axon terminal field areas (measured from the 2D convex hull). (a) Dendritic field area vs. axon terminal field area. Here and in (b–f), each data point corresponds to an individual cell (color-coded as indicated in inset above panels). The dashed line corresponds to the identity line, that is, identical area of dendritic field and axon terminal field. (b) As in (a), but with expanded range of axes to only include data points for rod bipolar cells. Notice that for all rod bipolar cells, the axon terminal field area is smaller than the dendritic field area. (c) Length of the axon terminal processes vs. axon terminal field area. (d) Length of the dendritic processes vs. dendritic field area. (e) Number of branch segments in the axon terminal vs. axon terminal field area. (f) Number of branch segments in the dendritic tree vs. dendritic field area

3.8 | Quantitative analysis of axon terminal varicosities

Varicosities appear as discrete swellings along the axon terminal branches and are a characteristic feature of all cone bipolar cells. They are thought to represent the major location of synaptic inputs and outputs, with inputs from amacrine cells and outputs to amacrine cells and ganglion cells (Boycott & Dowling, 1969; Cohen & Sterling, 1990; Kolb, 1979; McGuire et al., 1984; Strettoi et al., 1994). From the stratification analysis in Figure 7b, it can be seen that the distribution profiles of the average density of axon terminal varicosities for the different types of cone bipolar cells are fairly similar to the other branching properties analyzed. This suggests that, to the extent that varicosities are indeed the predominant sites of synaptic inputs and outputs, the distribution

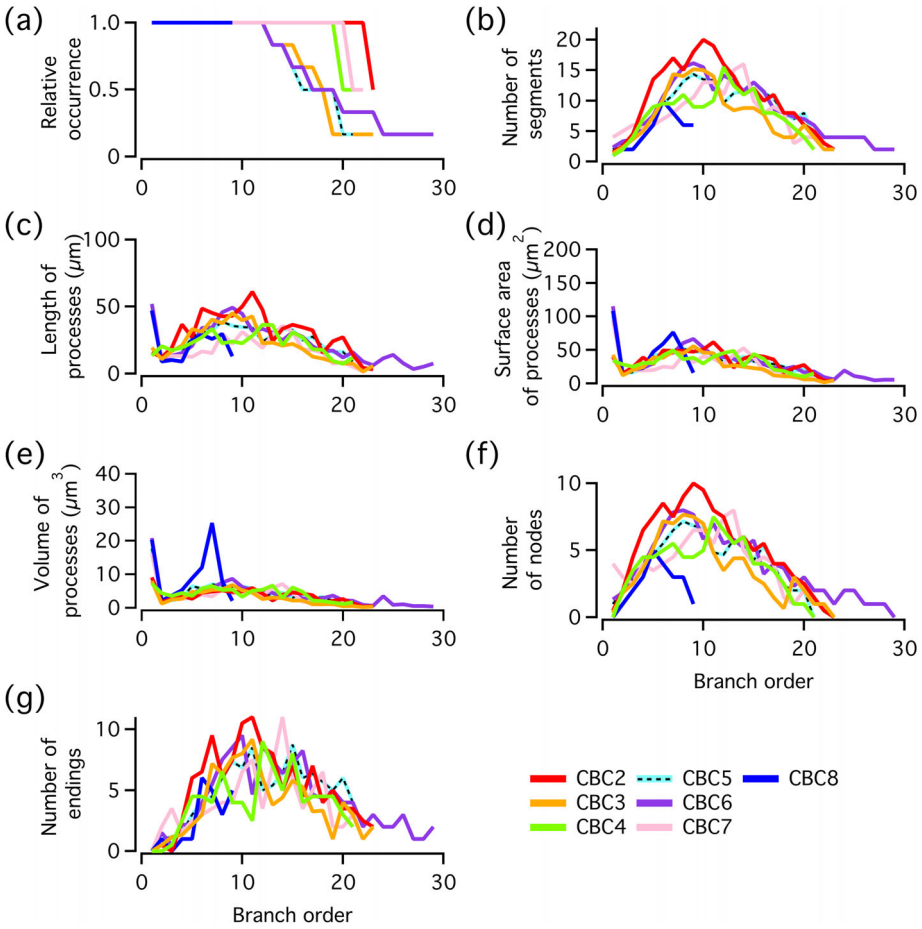

FIGURE 11 Axon parameters as a function of segment branch order for the central shaft branch ordering scheme for cone bipolar cells. (a) Relative occurrence of axon terminal segments of a given branch order for the different types of cone bipolar cells (CBC2–CBC8). Here and in (b–g), the color code is indicated in the inset below panels. All cone bipolar cells contained segments with branch order up to and including 9 and the highest branch order observed for any cell was 29. (b–g) Different axon parameters vs. branch order for the same cone bipolar cells as in (a). Data are plotted as lines between data points, with each data point corresponding to the average value for each cell type

of both branch length and surface area closely reflects the region over which a bipolar cell can interact directly with its pre- and postsynaptic partners.

In addition to the distribution across the IPL, we also analyzed the size of the axon terminal varicosities, measured as the diameter of the largest sphere that could be fitted within the largest projection of a given varicosity onto the XY plane. Figure 12 illustrates the distribution of varicosity diameters as a function of IPL depth for the different types of cone bipolar cells. The large majority of varicosities had a diameter between ~0.25 and ~1.25 μm, with essentially no difference between different cells within a given type (Figure 12a–g) or between different cone bipolar cell types (Figure 12h). Following from these observations, there was also no marked difference between varicosities located at different IPL depths (Figure 12a–h).

3.9 | Sholl analysis of the axon terminal

In addition to examining the morphological properties of bipolar cell axon terminals as a function of the stratification level in the IPL, we also analyzed a number of morphological properties as a function of local eccentricity, that is, relative to the center of the axon terminal. For this, we used Sholl analysis, with the concentric Sholl spheres centered at the transition point between the end of axon shaft and the start of the axon terminal (Figure 13a; see Materials and Methods). This differs from conventional Sholl analysis, where the spheres are centered at the cell body.

For the total population of reconstructed cone bipolar cells, the average radius of the outermost sphere was 26.4 ± 6.3 μm (range 17–41 μm), with no difference between ON- and OFF-cone bipolar cells (ON: 24.9 ± 6.4 μm, range 17–41 μm, $n = 15$; OFF: 28.7 ± 5.9 μm, range 21–41 μm; $n = 10$; $p = .1475$, unpaired t test). As expected, for rod bipolar cells, the average radius of the outermost sphere was lower: 16.5 ± 3.4 μm (range 12–25 μm, $n = 14$). For cone bipolar cells, the relative occurrence of Sholl sphere intersections (crossings) dropped below 1 in the range between 20 and 30 μm (Figure 13b). The number of intersections peaked at a Sholl radius of 10–20 μm, with only minor differences between the different types of cone bipolar cells (Figure 13c). When process length, surface area, volume, number of nodes, and number of endings were analyzed in the same

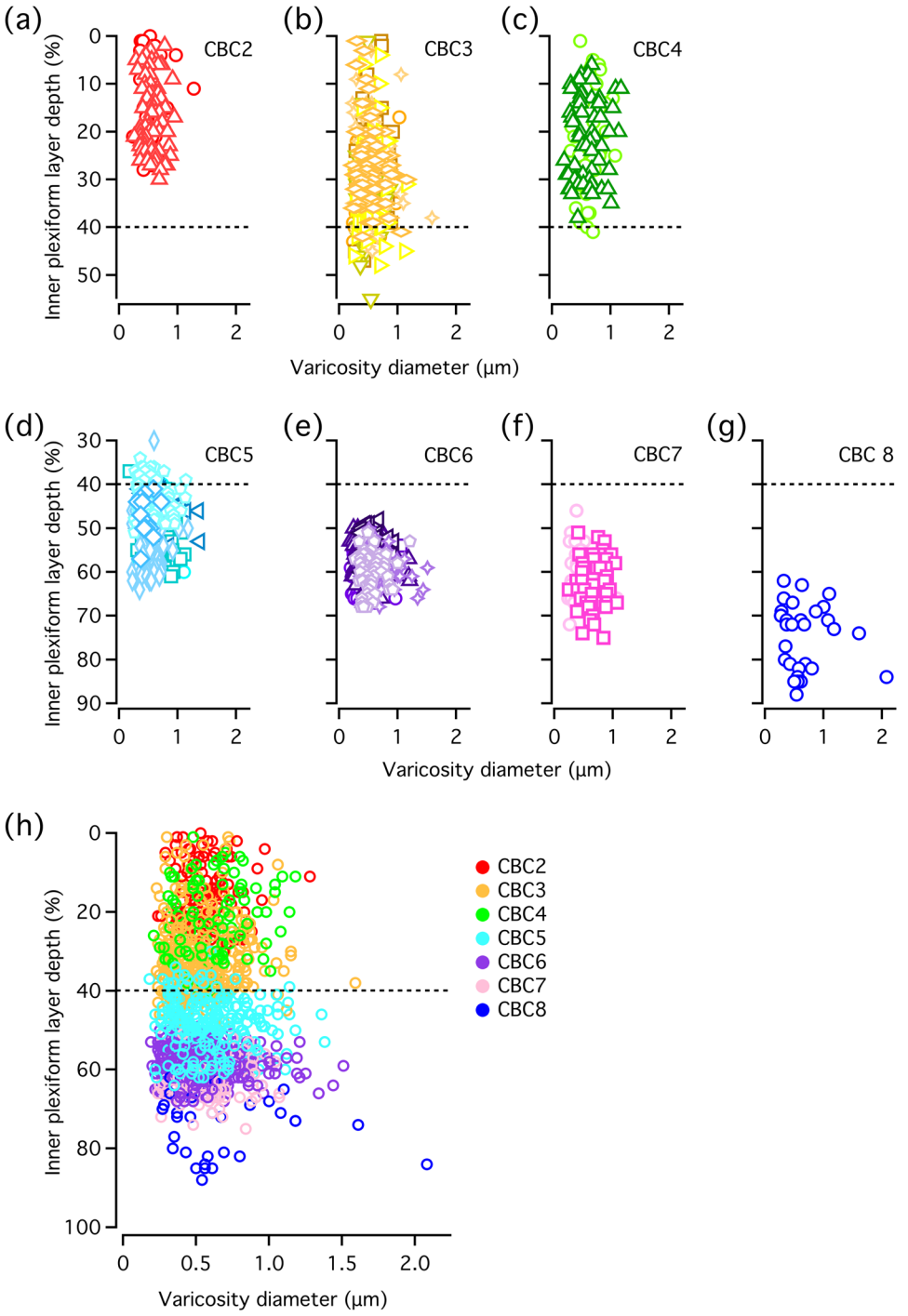

FIGURE 12 Size and distribution of axon terminal varicosities in the IPL for the different types of cone bipolar cells. (a–g) Location in the IPL (expressed as relative depth) vs. varicosity size for all varicosities for all cells of a given type of cone bipolar cell (n = number of cells): CBC2 ($n = 2$), CBC3 ($n = 6$), CBC4 ($n = 2$), CBC5 ($n = 6$), CBC6 ($n = 6$), CBC7 ($n = 2$), and CBC8 ($n = 1$). The size of a varicosity was determined as the diameter of the largest circle that would fit inside the varicosity in the XY plane (see Materials and Methods). Each data point corresponds to an individual varicosity and the data points for a given cell are identical with respect to shape and color saturation. (h) Overlay of data points for all varicosities of all cone bipolar cells (as in [a–g]). The data points for a given cell type are identical (color code indicated in inset)

way, there was considerable overlap between the different types of cells (Figure 13d–h). For CBC2–CBC7, the average process diameter as a function of Sholl radius appeared essentially indistinguishable, with a tendency toward a gradual reduction with increasing Sholl radius (Figure 13i). For CBC8, we observed a different profile with overall larger average diameters, but we only had data for one cell (Figure 13i). The distribution of the number of varicosities as a function of Sholl radius also appeared very similar between the different types of cone bipolars, with a maximum between 10 and 20 μm (Figure 13j).

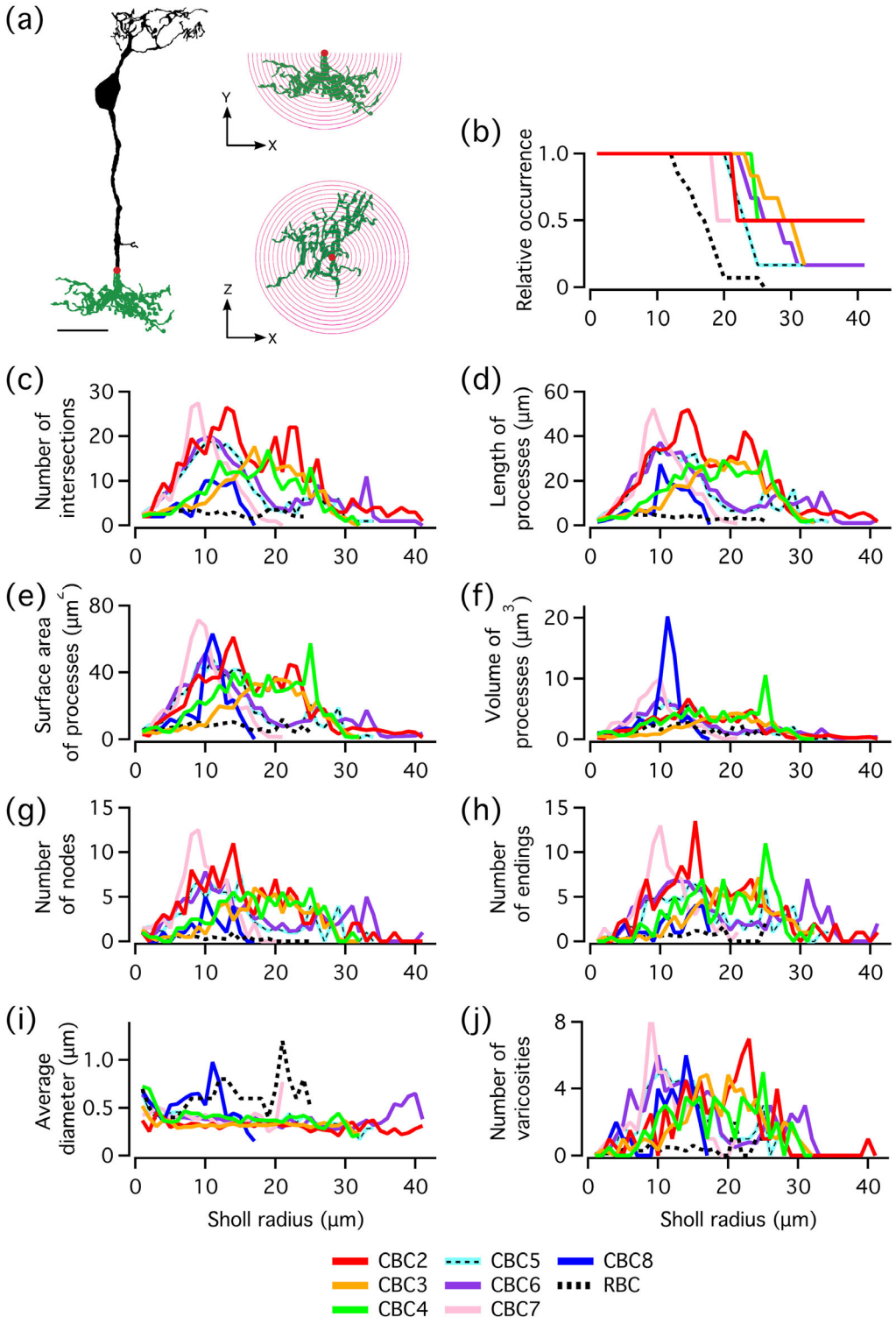

FIGURE 13 Sholl analysis of axon terminals of cone and rod bipolar cells. (a) Left: Shape plot of cone bipolar cell illustrates how the axon is composed of an axon shaft (black) and an axon terminal (green). Right (top and bottom): For the Sholl analysis, a set of nested concentric spheres (1 μm separation) were centered at the start of the axon terminal, that is, the point of transition between axon shaft and axon terminal (marked by red dot; see Materials and Methods). For clarity, 2D projections of axon terminal (green) are displayed in two different planes (XY and XZ), overlaid with cross sections of Sholl spheres (red lines). (b) Relative occurrence of Sholl spheres crossed by processes at a given distance from the start of the axon terminal for the different types of bipolar cells. (c–j) Different morphological parameters, counted either as a crossing with a specific sphere or contained in the shell between two neighboring spheres, as a function of Sholl sphere radius. Data are plotted as mean values for each cell type

3.10 | Relationship between arbor volume and branch density

In a study that investigated multiple types of neurons, Teeter and Stevens (2011) reported a general structural design (scaling) principle of neural arbors. They observed that an increase in territory size was accompanied by a systematic decrease in arbor density. To analyze this for dendrites and axon terminals of bipolar cells, we calculated the average branch density as the total branch length divided by the territory volume, with the latter defined by the volume of the corresponding 3D convex hull (calculated separately for the dendrites and axon terminal of each cell). For both the dendrites (Figure 14a) and the axon terminals (Figure 14b), there was an inverse relationship between the convex hull volume and the branch density. When we analyzed the relationship in logarithmic space and fitted the relationship with a straight line, the slope was -0.44 for the dendritic branches (Figure 14a) and -0.33 for the axon terminal branches (Figure 14b). In both cases, this corresponds to an exponent in linear space (cf. Teeter & Stevens, 2011). These results suggest that bipolar cells adhere to the general design principle where branching density decreases as arbor territory increases. Compared to the relationship reported by Teeter and Stevens (2011), however, the bipolar cells consistently displayed a higher branch density for a given convex hull volume (Figure 14). This was observed for both dendritic and axon terminal arbors.

3.11 | Comparing morphology of rod bipolar cells visualized by MPE fluorescence microscopy or biocytin histology

In an earlier study from our laboratory, we filled rod bipolar cells (n = 10) in rat retinal slices with biocytin and reconstructed the morphology after histochemical detection (Oltedal et al., 2009). In the following, we compare the morphological properties of the cells in Oltedal et al. (2009; "earlier cells") and the current study. The total surface area was very similar for the two populations (525 ± 61 μm^2 for the earlier cells vs. 601 ± 120 μm^2 for the current cells). For the earlier cells, however, the average surface area of the cell bodies was larger and the average surface area of the dendritic processes was smaller than for the current cells. We think there are two reasons for these differences. First, in the Oltedal et al. (2009) study, cells in the outermost part of the INL were specifically targeted to maximize the likelihood of obtaining rod bipolar cells. In the current study, we typically targeted cells in the middle of the INL, with the intention of obtaining different types of cone bipolar cells. In addition to cone bipolar cells, however, we also obtained a number of rod bipolar cells with cell bodies located more proximally (vitread) in the INL. Several of these cells have a dendritic expansion closer to the OPL, appearing almost as a "satellite" soma-like structure from which the final dendritic tree sprouts (Figure 5). For the morphometric analysis, these structures were included as part of the dendritic tree. The selection bias introduced by targeting cells in the middle of the INL increased the proportion of such rod bipolar cells compared to Oltedal et al. (2009), resulting in a larger average dendritic surface area for the rod bipolar cells.

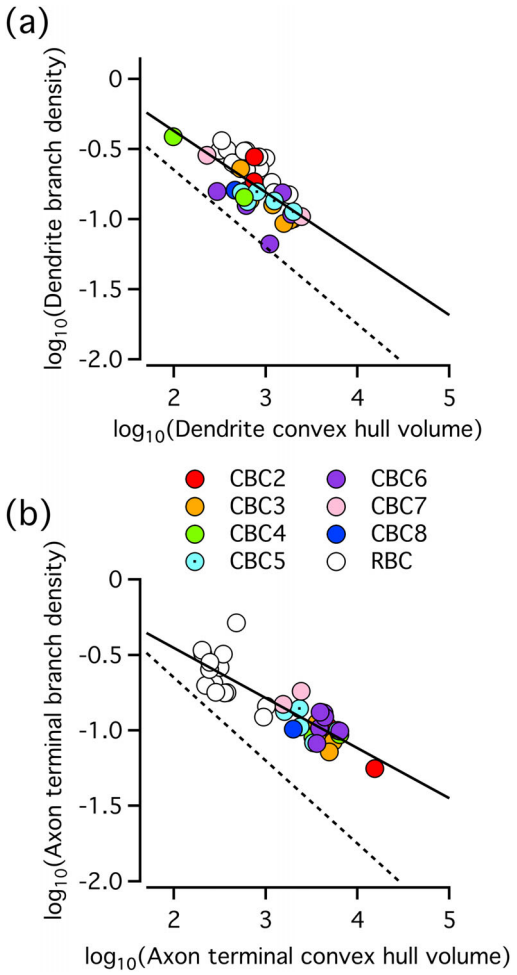

FIGURE 14 The relationship between arbor volume and branch density for dendritic trees and axon terminals of cone and rod bipolar cells (color code in inset between panels). (a) Dendritic branch density (defined as total dendritic branch length divided by the convex hull volume of the dendritic tree(s); in μm^{-2}) vs. convex hull volume (in μm^3) of the dendritic tree(s). Here and in (b), each data point corresponds to an individual cell. A straight line (continuous) has been fitted to the data points and has a slope of -0.44 and an intercept of 0.50. Here and in (b), the dashed line corresponds to the line fitted to the data points of Teeter and Stevens (2011), corresponding to dendritic trees of pyramidal neurons and interneurons from a variety of species, with a slope of −0.55 and an intercept of 0.45. (b) Axon terminal branch density (defined as total axon terminal branch length divided by the convex hull volume of the axon terminal; in μm^{-2}) vs. convex hull volume (in μm^3) of the axon terminal. A straight line (continuous) has been fitted to the data points and has a slope of -0.33 and an intercept of 0.21

Second, in the current study, the reconstructions of rod bipolar cells contain a larger number of dendritic endings and larger total dendritic length than in the earlier study. For comparison, Oltedal et al. (2009) reported 9.6 ± 3.7 dendritic endings and a total dendritic length of 46 ± 18 μm, whereas in the current study, we found 39 ± 12 endings and a total dendritic length of 175 ± 59 μm. When we compared the axon terminal processes, we found a smaller number of endings in the earlier (2.4 ± 0.8) than in the current (9.1 ± 3.5) reconstructions. Taken together, this is similar to a previous comparison between

reconstructions performed in our laboratory using MPE microscopy or tracer histochemistry for AII amacrine cells (Zandt et al., 2017). In both cases, it seems that the tissue processing involved in biocytin histology increases the risk of missing a number of thin processes during the subsequent reconstruction.

4 | DISCUSSION

In this study, we have used MPE microscopy to acquire image stacks of bipolar cells after filling them with fluorescent dye during whole-cell recording of visually targeted cells in rat retinal slices. After image deconvolution, we digitally and quantitatively reconstructed complete morphologies of the bipolar cells and performed detailed morphometric analysis to investigate which morphological properties can best be used for characterization and classification in experiments with combined structural and functional analysis. In the following, we will discuss the most important results and how they can be useful for future investigations of the relation between structure and function of retinal bipolar cells, including the development of compartmental models to study the functional importance of passive and active membrane properties of these cells for the signal processing that takes place during vision.

Our results also establish a database of morphometric properties of bipolar cells that can be of value for future studies of development, regeneration, degeneration, and disease processes. In particular, when pathological conditions evoke changes of cellular morphology, for example, during retinal remodeling, that can make it difficult to recognize specific cell types, comparing the morphology with the data reported here can contribute to detecting and quantifying the extent of such remodeling.

4.1 | Quantitative morphological analysis of bipolar cells

Although the morphology of bipolar cells has been studied in a number of different mammalian retinas, there has been a surprising lack of quantitative information about morphological parameters, including the pattern and extent of branching of the axon terminals in the IPL. The "classical" studies were based on Golgi impregnation (Boycott & Dowling, 1969; Boycott & Wässle, 1991; Cajal, 1893, 1894, 1911; Dacheux & Raviola, 1986; Famiglietti, 1981; Linberg et al., 1996; MacNeil et al., 2004; Polyak, 1941; West, 1976, 1978) in a number of species (cat, dog, rabbit, ox, ground squirrel, primate, and human). However, more recent studies have investigated rodent retinas (rat and mouse) because of the ease with which morphological characterization can be combined with physiological recording and because the mouse has become the source of a rich variety of genetically manipulated lines (e.g., Strettoi et al., 2010).

Compared to illustrations of bipolar cells based on Golgi impregnation and wide-field fluorescence microscopy, the axon terminal branching observed for our reconstructed cells seems considerably more extensive. Older studies have often used simple hand drawings where the main focus most likely was to capture essential aspects of the morphology, without representing all details in a faithful manner. To our knowledge, no studies have performed quantitative morphological reconstructions of dye-filled bipolar cells after imaging with confocal microscopy. Whereas previous studies with morphological reconstructions based on ultrastructural imaging with transmission EM probably suffered from a fair number of lost sections (e.g., Cohen & Sterling, 1990; McGuire et al., 1984), newer studies with deep connectomics, in particular the near-complete representations based on the SBFSEM technique applied to mouse bipolar cells (Behrens et al., 2016; Greene et al., 2016; Helmstaedter et al., 2013), seem to have generated axon terminal morphologies very similar to those obtained in our study. For extensive and detailed comparisons, it is a challenge that although the SBFSEM reconstructions are complete for the imaged volume of retinal tissue, most cells have been reconstructed only by their (center line) skeletons (Helmstaedter et al., 2013) as opposed to complete volumetric segmentation. Volumetric segmentation and reconstruction of EM material is also very important to constrain the diameters of the thinnest processes when they are below the limit of resolution of light microscopy, as is the case for many retinal neurons. In the current study, we used EM data to guide the reconstruction of thin dendritic branches and the intervaricosity segments of axon terminal branches.

Our morphological reconstructions of several cone bipolar cells allowed comparison of the size of the dendritic field in the OPL and the axon terminal field in the IPL. From a detailed study of the tiling of the retinal surface by different types of cone bipolar cells in mouse retina, Wässle et al. (2009) concluded that the coverage factors for the axonal and dendritic fields for cell types considered to be homogeneous were close to 1, that is, with little overlap and no "missed" regions between cells. In a recent study of mouse bipolar cells, Behrens et al. (2016) reported that for most cone bipolar cell types, the coverage factors for dendritic and axon terminal fields were moderately larger than 1, and generally larger for the axonal than for the dendritic fields. Unfortunately, however, the authors did not provide information about the areas of the dendritic and axon terminal fields for individual bipolar cells. In our study, we typically found that the area of the axon terminal fields (measured as the area of the 2D convex hull in the plane of the retina) was consistently larger than the area of the dendritic field. For most cells, the difference was moderate and we suspect that for the small number of cells where the dendritic field was much smaller than the axonal field, the dendrites may have been truncated during slice preparation. To understand the extent of this variability, it will be necessary to obtain data for a larger number of cells in multiple regions across the intact retina.

4.2 | Classification of bipolar cells

Whereas the distinction between rod and cone bipolar cells, as well as the existence of different types of cone bipolar cells, were clearly recognized by Cajal (1893, 1894, 1911), it was Polyak (1941) who initiated a systematic classification of the different types of cone bipolar cells,

as studied in the primate retina. For rat retina, the initial characterization and classification of different types of cone bipolar cells (CBC1–CBC9) was based on wide-field fluorescence microscopy of cells in retinal slices injected with fluorescent dyes using sharp microelectrodes (Euler & Wässle, 1995). Subsequent investigations both confirmed (Hartveit, 1997) and extended the classification by proposing the existence of additional cell types (Cui & Pan, 2008; Ivanova & Müller, 2006). Ivanova and Müller (2006) suggested that type CBC6 should be split into two different types (CBC6a and CBC6b) with different morphological (CBC6a with narrowly stratifying and CBC6b with broadly stratifying axon terminals, respectively) and physiological properties (differential expression of HCN channels). Subsequent investigations of rat retina have suggested potential redefinitions of several types of cone bipolar cells. First, that CBC5 should be split into two different types (CBC5a and CBC5b), based on differences in the expression of HCN channels and voltage-gated Na^+ and Ca^{2+} channels (Cui & Pan, 2008; Fyk-Kolodziej & Pourcho, 2007). More recently, Vielma and Schmachtenberg (2016) suggested that CBC3 should be split into two types (CBC3a and CBC3b) and that, potentially, the same should be done for CBC2 (CBC2 and CBC2'), with reclassification primarily based on differences in physiological response properties. Despite the strong evidence provided by these studies for variability of physiological response properties and ion channel expression patterns, it is less clear that the observed differences correspond to clear morphological differences and that they constitute a strong basis on which to propose the existence of different cell types that independently tile the retina.

The suggestions for redefining the classification of cone bipolar cells in rat retina have been paralleled by corresponding investigations in mouse retina, but with an overall stronger justification. First, in their initial classification study, Ghosh et al. (2004) noted considerable variability in the axonal ramification pattern of CBC5 and in a subsequent study from the same laboratory, Wässle et al. (2009) proposed a split of CBC5 into two separate types. In an immunolabeling study, Mataruga et al. (2007) split CBC3 into two separate types, termed CBC3a and CBC3b. These reclassifications were supported by a more recent ultrastructural connectomics study (Helmstaedter et al., 2013) that split both CBC3 and CBC5. CBC3 was split into CBC3a and CBC3b, presumably identical to CBC3a and CBC3b of Mataruga et al. (2007). CBC5 was split into two (potentially three) different types. In addition, Helmstaedter et al. (2013) described a new type termed "XBC" or CBC-X. Shortly after, Greene et al. (2016) distinguished between CBC5i, CBC5o, and CBC5t, with subtle differences in the stratification pattern of the axon terminals in the IPL. These types were verified and recognized by Tsukamoto and Omi (2017) who proposed an alternative nomenclature (CBC5i = CBC5a, CBC5o = CBC5b, CBC5t = CBC5c) and renamed CBC-X to CBC5d. For these studies, the classification of a population of cells within a retinal tissue volume was strongly improved by the complete skeleton reconstructions, which permitted tiling violations to be observed, thereby guiding (re)classification of cells with subtle differences in the stratification patterns. Although ultrastructural connectomics remains unsurpassed with respect to complete classification of cells within a small tissue volume, progress has been slow regarding the parallel investigation of physiological response properties, in particular the characterization of physiological response properties that can provide mechanistic insight into the basis for differences in visual response properties. Unfortunately, the technical difficulty of the required investigations is compounded by the fact that although mouse and rat cone bipolar cells follow the same overall naming conventions (CBC1–CBC9), the different types in one species may not have consistent corresponding partners in the other species. Even for types with morphological similarity between species, it cannot be taken for granted that their physiological properties and expression patterns of relevant ion channels are identical.

In our study, we searched extensively for morphological characteristics and parameters that could serve as "markers," with quantitative differences between types sufficient to contribute to classification of individual cells in future investigations. Perhaps unsurprisingly, the only consistent and (relatively) robust morphological difference is the level and thickness of the stratification of the axon terminals in the IPL. With future advances in classification of cone bipolar cells, including potential reclassifications as discussed above, it is an open question whether determining the axon terminal stratification will be sufficient for accurately classifying individual bipolar cells. We believe, however, that the increased resolution offered by MPE microscopy of cells filled with fluorescent dye, combined with quantitative morphological reconstruction and correlated MPE microscopy and IR-LSGC imaging, will facilitate future experimental investigations that combine electrophysiological recording and imaging. An important point is that offline processing with digital rotation of the image stack and the corresponding morphological reconstruction can reduce the likelihood of misclassification.

In mouse retina, the strongest basis for increasing the number of bipolar cell types (including splitting pre-existing types) has come from methodological advances exemplified by high-resolution ultrastructural imaging (SBFSEM; Greene et al., 2016; Helmstaedter et al., 2013) and from large-scale genetic profiling (Shekhar et al., 2016), with good internal consistency between the different studies. Shekhar et al. (2016) identified a number of genes that differed in their expression between the different types of bipolar cells, but the potential relation and contribution to differences in physiological properties is still not resolved. However, to understand how the different visual response properties of bipolar cells are generated, we will need detailed correlative studies that examine passive and active membrane properties of specific cell types.

4.3 | Correlating structure and function of bipolar cells

Although connectivity is fundamental, it is not everything (cf. Seung & Sümbül, 2014) and in addition to the structural information, we need information about passive and active membrane properties, including the identity, localization, and functional properties of ion channels and synaptic receptors. It is a considerable challenge, however, to correlate the structure and function of cone bipolar cells, even with the advent

of a variety of distinct mouse lines with genetically labeled cell types (e.g., Breuninger et al., 2011). It is currently possible to perform electrophysiological recording from visually targeted cells only for some types of cone bipolar cells with distinct fluorescent labels. If experiments are instead performed on wild-type mice without genetically labeled cell types, it is unknown if all the different types of cone bipolar cells suggested to be present in mouse retina can be identified based on morphological properties, for example, stratification in the IPL. Importantly, it is not a prerequisite that a cell's identity must be determined during the experiment itself. It is sufficient if the morphological data can be acquired during the experiment, potentially in parallel with physiological measurements, as long as the imaging technique is compatible with physiological recording. It will be interesting to see if complete ultrastructural reconstruction can be applied routinely in combination with whole-cell recording in physiological experiments. Currently, it seems unlikely that deep connectomics can replace light microscopic imaging anytime soon.

4.4 | The rat retina as an experimental system for investigating bipolar cells

As discussed above, the potential availability of mouse lines with genetically labeled cell types makes this species a very useful model system for studies of the mammalian retina. Nevertheless, this needs to be weighed against advantages and disadvantages of alternative model systems. At this time, the rat retina has some advantages as a model system for investigating cone bipolar cells. First, compared to mouse, voltage-gated ion channels have been more extensively characterized in rat cone bipolar cells, for example, I_{Na} (Cui & Pan, 2008; Ivanova & Müller, 2006), I_K (Ma et al., 2003, 2005), I_{Ca} (Hartveit, 1999; Hu et al., 2009; Pan, 2000; Protti & Llano, 1998), and I_h (Cui & Pan, 2008; Ivanova & Müller, 2006; Vielma & Schmachtenberg, 2016). In addition, the rat retina has been used extensively as a model in studies of retinal diseases, including diabetic retinopathy and glaucoma (e.g., Gallego-Ortega et al., 2020; Park et al., 2014). The competitive advantage of mouse retina based on multiple lines with genetically labeled cell types may also shift with recent development of CRISPR-Cas9 transgenic rats (e.g., Bäck et al., 2019).

4.5 | Morphological reconstruction for compartmental modeling

It was an explicit goal of the present study to establish a workflow for MPE microscopy of bipolar cells filled with fluorescent dye during whole-cell recording that can be extended to encompass compartmental modeling. For high-quality models, it is imperative that the morphological reconstructions are generated from the same neurons from which electrophysiological data are obtained (Carnevale & Hines, 2006; Holmes, 2010; Major, 2001). The published reconstructions generated from deep connectomics data without accompanying physiological data (e.g., Greene et al., 2016; Helmstaedter et al., 2013) are inadequate for high-quality compartmental modeling. Our laboratory has previously used MPE microscopy of cells filled with fluorescent dye during whole-cell recording to study the morphology of AII amacrine cells (Zandt et al., 2017, 2018). For typical microscope hardware, confocal microscopy can provide higher spatial resolution than MPE microscopy, but involves high phototoxicity and is better suited for imaging of fixed tissue slices after the physiological recording. This additional step adds the risk of losing or destroying valuable material, however, and it is often difficult to maintain an optimal orientation of the retinal slice for imaging. A well-established advantage of performing MPE imaging during the physiological experiment, compared to filling cells with tracer and processing slices after fixation (either by coupling the tracer with fluorescent dyes or by developing a visible reaction product), is that it completely avoids the shrinkage accompanying tissue fixation. To varying extents, such shrinkage always occurs during fixation and histological processing and can compromise the accuracy of cell reconstructions (Groh & Krieger, 2011; Jaeger, 2001). For small neurons like retinal bipolar cells, it is straightforward to acquire the complete morphology at sufficiently high resolution for Nyquist sampling in a single image stack.

ACKNOWLEDGMENTS

We thank Torhild Fjordheim Sunde and Áurea Castilho for excellent technical assistance.

CONFLICT OF INTEREST

The authors have nothing to disclose.

AUTHOR CONTRIBUTIONS

RF performed morphological reconstruction and morphometric analysis. RF and EH developed software for morphological analysis. MLV and EH performed electrophysiological recording and multiphoton excitation microscopy. MLV and EH conceived and designed experiments, supervised the project, and interpreted data. MLV and EH wrote the manuscript. RF, MLV, and EH made the figures. All authors commented on and approved the final version of the manuscript.

DATA AVAILABILITY STATEMENT

Raw data will be made available to researchers interested in them upon reasonable request, in accordance with journal policy.

PEER REVIEW

The peer review history for this article is available at https://publons.com/publon/10.1002/cne.25308.

ORCID

Rémi Fournel https://orcid.org/0000-0003-2486-0307
Margaret L. Veruki https://orcid.org/0000-0002-0532-144X
Espen Hartveit https://orcid.org/0000-0003-1798-1901

REFERENCES

Bäck, S., Necarsulmer, J., Whitaker, L. R., Coke, L. M., Koivula, P., Heathward, E. J., Fortuno, L. V., Zhang, Y., Yeh, C. G., Baldwin, H. A., Spencer, M. D., Mejias-Aponte, C. A., Pickel, J., Hoffman, A. F., Spivak, C. E., Lupica, C. R., Underhill, S. M., Amara, S. G., Domanskyi, A., …, & Harvey, B. K.

(2019). Neuron-specific genome modification in the adult rat brain using CRISPR-Cas9 transgenic rats. *Neuron*, *102*, 105–119.

Behrens, C., Schubert, T., Haverkamp, S., Euler, T., & Berens, P. (2016). Connectivity map of bipolar cells and photoreceptors in the mouse retina. *eLife*, *5*. pii: e20041.

Boycott, B. B., & Dowling, J. E. (1969). Organization of the primate retina: Light microscopy. *Philosophical Transactions of the Royal Society of London, Series B, Biological Sciences*, *255*, 109–194.

Boycott, B. B., & Wässle, H. (1991) Morphological classification of bipolar cells of the primate retina. *European Journal of Neuroscience*, *3*, 1069–1088.

Brandstätter, J. H., Dick, O., & Boeckers, T. M. (2004). The postsynaptic scaffold proteins ProSAP1/Shank2 and Homer1 are associated with glutamate receptor complexes at rat retinal synapses. *Journal of Comparative Neurology*, *475*, 551–563.

Breuninger, T., Puller, C., Haverkamp, S., & Euler, T. (2011). Chromatic bipolar cell pathways in the mouse retina. *Journal of Neuroscience*, *31*, 6504–6517.

Cajal, S. R. y (1893). La rétine des vertébrés. *La Cellule*, *9*, 119–257. English translation in *The Structure of the Retina* (1972), compiled and translated by S. A. Thorpe & M. Glickstein. Springfield, IL: Charles C. Thomas.

Cajal, S. R. y (1894). *Les Nouvelles Idées sur la Structure du Système Nerveux chez l'Homme et chez les Vertébrés*. Paris: Reinwald & C^{ie}. English translation in *New Ideas on the Structure of the Nervous System in Man and Vertebrates* (1990), translated by N. Swanson & L. W. Swanson. Cambridge, MA: MIT Press.

Cajal, S. R. y (1911). *Histologie du Système Nerveux de l'Homme et des Vertébrés* (vol., II). Paris: Maloine. English translation in *Histology of the Nervous System of Man and Vertebrates*, Vol. II (1995), translated by N. Swanson & L. W. Swanson. New York, NY: Oxford University Press.

Cao, Y., Sarria, I., Fehlhaber, K. E., Kamasawa, N., Orlandi, C., James, K. N., Hazen, J. L., Gardner, M. R., Farzan, M., Lee, A., Baker, S., Baldwin, K., Sampath, A. P., & Martemyanov, K. A. (2015). Mechanism for selective synaptic wiring of rod photoreceptors into the retinal circuitry and its role in vision. *Neuron*, *87*, 1248–1260.

Capowski, J. J. (1989). *Computer techniques in neuroanatomy*. New York and London: Plenum Press.

Carnevale, N. T., & Hines, M. L. (2006). *The NEURON book*. Cambridge: Cambridge University Press.

Chun, M.-H., Han, S.-H., Chung, J.-W., & Wässle, H. (1993). Electron microscopic analysis of the rod pathway of the rat retina. *Journal of Comparative Neurology*, *332*, 421–432.

Chun, M.-H., Oh, S.-J., Kim, I.-B., & Kim, K.-Y. (1999). Light and electron microscopical analysis of nitric oxide synthase-like immunoreactive neurons in the rat retina. *Visual Neuroscience*, *16*, 379–389.

Cohen, E., & Sterling, P. (1990). Demonstration of cell types among cone bipolar neurons of cat retina. *Philosophical Transactions of the Royal Society of London, Series B, Biological Sciences*, *330*, 305–321.

Cui, J., & Pan, Z.-H. (2008). Two types of cone bipolar cells express voltage-gated Na^+ channels in the rat retina. *Visual Neuroscience*, *25*, 635–645.

Dacheux, R. F., & Raviola, E. (1986). The rod pathway in the rabit retina: A depolarizing bipolar and amacrine cell. *Journal of Neuroscience*, *6*, 331–345.

Dowling, J. E., & Boycott, B. B. (1966). Organization of the primate retina: Electron microscopy. *Proceedings of the Royal Society of London, Series B, Biological Sciences*, *166*, 80–111.

Euler, T., & Wässle, H. (1995). Immunocytochemical identification of cone bipolar cells in the rat retina. *Journal of Comparative Neurology*, *361*, 461–478.

Euler, T., Schneider, H., & Wässle, H. (1996). Glutamate responses of bipolar cells in a slice preparation of the rat retina. *Journal of Neuroscience*, *16*, 2934–2944.

Euler, T., Haverkamp, S., Schubert, T., & Baden, T. (2014). Retinal bipolar cells: Elementary building blocks of vision. *Nature Reviews Neuroscience*, *15*, 507–519.

Famiglietti, E. V. (1981). Functional architecture of cone bipolar cells in mammalian retina. *Vision Research*, *21*, 1559–1563.

Famiglietti, E. V., & Kolb, H. (1976). Structural basis for ON-and OFF-center responses in retinal ganglion cells. *Science*, *194*, 193–195.

Franke, K., Berens, P., Schubert, T., Bethge, M., Euler, T., & Baden, T. (2017). Inhibition decorrelates visual feature representations in the inner retina. *Nature*, *542*, 439–444.

Fyk-Kolodziej, B., & Pourcho, R. G. (2007). Differential distribution of hyperpolarization-activated and cyclic nucleotide-gated channels in cone bipolar cells of the rat retina. *Journal of Comparative Neurology*, *501*, 891–903.

Gallego-Ortega, A., Norte-Muñoz, M., Miralles de Imperial-Ollero, J. A., Bernal-Garro, J. M., Valiente-Soriano, F. J., de la Villa Polo, P., Avilés-Trigueros, M., Villegas-Pérez, M. P., & Vidal-Sanz, M. (2020). Functional and morphological alterations in a glaucoma model of acute ocular hypertension. *Progress in Brain Research*, *256*, 1–29.

Ghosh, K., Bujan, S., Haverkamp, S., Feigenspan, A., & Wässle, H. (2004). Types of bipolar cells in the mouse retina. *Journal of Comparative Neurology*, *469*, 70–82.

Golgi, C. (1873). Sulla struttura della sostanza grigia del cervello (Communicazione preventiva). *Gazzetta Medica Italiana*, *33*, 244–246. Reprinted as: Sulla sostanza grigia del cervello, *Opera Omnia*, 1903, Vol. 1, *Istologia Normale*, pp. 91–98. Milan, Italy: Ulrico Hoepli.

Greene, M. J., Kim, J. S., Seung, H. S., & EyeWirers (2016). Analogous convergence of sustained and transient inputs in parallel on and off pathways for retinal motion computation. *Cell Reports*, *14*, 1892–1900.

Greferath, U., Grünert, U., & Wässle, H. (1990). Rod bipolar cells in the mammalian retina show protein kinase C-like immunoreactivity. *Journal of Comparative Neurology*, *301*, 433–442.

Groh, A., & Krieger, P. (2011). Structure–function analysis of genetically defined neuronal populations. In: Helmchen, F., & Konnerth, A. Series ed. Yuste, R. *Imaging in neuroscience* (pp. 377–386). Cold Spring Harbor, NY: Cold Spring Harbor Laboratory Press.

Hartveit, E. (1997). Functional organization of cone bipolar cells in the rat retina. *Journal of Neurophysiology*, *77*, 1716–1730.

Hartveit, E. (1999). Reciprocal synaptic interactions between rod bipolar cells and amacrine cells in the rat retina. *Journal of Neurophysiology*, *81*, 2923–2936.

Haverkamp, S., Specht, D., Majumdar, S., Zaidi, N. F., Brandstätter, J. H., Wasco, W., Wässle, H., & Tom Dieck, S. (2008). Type 4 OFF cone bipolar cells of the mouse retina express calsenilin and contact cones as well as rods. *Journal of Comparative Neurology*, *507*, 1087–1101.

Hellmer, C. B., Zhou, Y., Fyk-Kolodziej, B., Hu, Z., & Ichinose, T. (2016). Morphological and physiological analysis of type-5 and other bipolar cells in the mouse retina. *Neuroscience*, *315*, 246–258.

Helmstaedter, M., Briggman, K. L., Turaga, S. C., Jain, V., Seung, H. S., & Denk, W. (2013). Connectomic reconstruction of the inner plexiform layer in the mouse retina. *Nature*, *500*, 168–174.

Holmes, W. R. (2010). Passive cable modeling. In: De Schutter, E. (Ed.), *Computational modeling methods for neuroscientists* (pp. 233–258). Cambridge, MA: MIT Press.

Hu, C., Bi, A., & Pan, Z.-H. (2009). Differential expression of three T-type calcium channels in retinal bipolar cells in rats. *Visual Neuroscience*, *26*, 177–187.

Ichinose, T., Fyk-Kolodziej, B., & Cohn, J. (2014). Roles of ON cone bipolar cell subtypes in temporal coding in the mouse retina. *Journal of Neuroscience*, *34*, 8761–8771.

Ivanova, E., & Müller, F. (2006). Retinal bipolar cell types differ in their inventory of ion channels. *Visual Neuroscience*, *23*, 143–154.

Jaeger, D. (2001). Accurate reconstruction of neuronal morphology. In: De Schutter, E. (Ed.). *Computational neuroscience. Realistic modeling for experimentalists* (pp. 159–178). Boca Raton, FL: CRC Press.

Keeley, P. W., & Reese, B. E. (2010). Role of afferents in the differentiation of bipolar cells in the mouse retina. *Journal of Neuroscience*, *30*, 1677–1685.

Kolb, H. (1979). The inner plexiform layer in the retina of the cat: Electron microscopic observations. *Journal of Neurocytology*, *8*, 295–329.

Koulen, P., Kuhn, R., Wässle, H., & Brandstätter, J. H. (1997). Group I metabotropic glutamate receptors mGluR1alpha and mGluR5a: Localization in both synaptic layers of the rat retina. *Journal of Neuroscience*, *17*, 2200–2211.

Light, A. C., Zhu, Y., Shi, J., Saszik, S., Lindstrom, S., Davidson, L., Li, X., Chiodo, V. A., Hauswirth, W. W., Li, W., & DeVries, S. H. (2012). Organizational motifs for ground squirrel cone bipolar cells. *Journal of Comparative Neurology*, *520*, 2864–2887.

Linberg, K. A., Suemune, S., & Fisher, S. K. (1996). Retinal neurons of the California ground squirrel, *Spermopilus beecheyi*: A Golgi study. *Journal of Comparative Neurology*, *365*, 173–216.

Ma, Y.-P., Cui, J., Hu, H.-J., & Pan, Z.-H. (2003). Mammalian retinal bipolar cells express inwardly rectifying K^+ currents (I_{Kir}) with a different distribution than that of I_h. *Journal of Neurophysiology*, *90*, 3479–3489.

Ma, Y.-P., Cui, J., & Pan, Z.-H. (2005). Heterogeneous expression of voltage-dependent Na^+ and K^+ channels in mammalian retinal bipolar cells. *Visual Neuroscience*, *22*, 119–133.

MacNeil, M. A., Heussy, J. K., Dacheux, R. F., Raviola, E., & Masland, R. H. (2004). The population of bipolar cells in the rabbit retina. *Journal of Comparative Neurology*, *472*, 73–86.

Major, G. (2001). Passive cable modeling — A practical introduction. In: De Schutter, E. (Ed.), *Computational neuroscience. Realistic modeling for experimentalists* (pp. 209–232). Boca Raton, FL: CRC Press.

Mataruga, A., Kremmer, E., & Müller, F. (2007). Type 3a and type 3b OFF cone bipolar cells provide for the alternative rod pathway in the mouse retina. *Journal of Comparative Neurology*, *502*, 1123–1137.

McGuire, B. A., Stevens, J. K., & Sterling, P. (1984). Microcircuitry of bipolar cells in cat retina. *Journal of Neuroscience*, *4*, 2920–2938.

Oltedal, L., Veruki, M. L., & Hartveit, E. (2009). Passive membrane properties and electrotonic signal processing in retinal rod bipolar cells. *Journal of Physiology*, *587*, 829–849.

Pan, Z.-H. (2000). Differential expression of high- and two types of low-voltage-activated calcium currents in rod and cone bipolar cells of the rat retina. *Journal of Neurophysiology*, *83*, 513–527.

Park, H. Y., Kim, J. H., & Park, C. K. (2014). Alterations of the synapse of the inner retinal layers after chronic intraocular pressure elevation in glaucoma animal model. *Molecular Brain*, *7*, 53.

Pignatelli, V., & Strettoi, E. (2004). Bipolar cells of the mouse retina: A gene gun, morphological study. *Journal of Comparative Morphology*, *476*, 254–266.

Polyak, S. L. (1941). *The retina*. Chicago, IL: Chicago University Press.

Protti, D. A., & Llano, I. (1998). Calcium currents and calcium signaling in rod bipolar cells of rat retinal slices. *Journal of Neuroscience*, *18*, 3715–3724.

Sassoè-Pognetto, M., Wässle, H., & Grunert, U. (1994). Glycinergic synapses in the rod pathway of the rat retina: Cone bipolar cells express the alpha 1 subunit of the glycine receptor. *Journal of Neuroscience*, *14*, 5131–5146.

Scorcioni, R., Polavaram, S., & Ascoli, G. A. (2008). L-measure: A web-accessible tool for the analysis, comparison and search of digital reconstructions of neuronal morphologies. *Nature Protocols*, *3*, 866–876.

Seung, H. S., & Sümbül, U. (2014). Neuronal cell types and connectivity: Lessons from the retina. *Neuron*, *83*, 1262–1272.

Shekhar, K., Lapan, S. W., Whitney, I. E., Tran, N. M., Macosko, E. Z., Kowalczyk, M., Adiconis, X., Levin, J. Z., Nemesh, J., Goldman, M., McCarroll, S. A., Cepko, C. L., Regev, A., & Sanes, J. R. (2016). Comprehensive classification of retinal bipolar neurons by single-cell transcriptomics. *Cell*, *166*, 1308–1323.

Sholl, D. A. (1953). Dendritic organization in the neurons of the visual and motor cortices of the cat. *Journal of Anatomy*, *87*, 387–406.

Sterling, P. (1983). Microcircuitry of the cat retina. *Annual Review of Neuroscience*, *6*, 149–185.

Strettoi, E., Dacheux, R. F., & Raviola, E. (1994). Cone bipolar cells as interneurons in the rod pathway of the rabbit retina. *Journal of Comparative Neurology*, *347*, 139–149.

Strettoi, E., Novelli, E., Mazzoni, F., Barone, I., & Damiani, D. (2010). Complexity of retinal cone bipolar cells. *Progress in Retinal and Eye Research*, *29*, 272–283.

Szél, Á., & Röhlich, P. (1992). Two cone types of rat retina detected by anti-visual pigment antibodies. *Experimental Eye Research*, *55*, 47–52.

Teeter, C. M., & Stevens, C. F. (2011). A general principle of neural arbor branch density. *Current Biology*, *21*, 2105–2108.

Tsukamoto, Y., Morigiwa, K., Ueda, M., & Sterling, P. (2001). Microcircuits for night vision in mouse retina. *Journal of Neuroscience*, *21*, 8616–8623.

Tsukamoto, Y., & Omi, N. (2015). OFF bipolar cells in macaque retina: Type specific connectivity in the outer and inner synaptic layers. *Frontiers in Neuroanatomy*, *9*, 122.

Tsukamoto, Y., & Omi, N. (2017). Classification of mouse retinal bipolar cells: Type-specific connectivity with special reference to rod-driven AII amacrine pathways. *Frontiers in Neuroanatomy*, *11*, 92.

Vielma, A. H., & Schmachtenberg, O. (2016). Electrophysiological fingerprints of OFF bipolar cells in rat retina. *Scientific Reports*, *6*, 30259.

Wässle, H., Puller, C., Müller, F., & Haverkamp, S. (2009). Cone contacts, mosaics, and territories of bipolar cells in the mouse retina. *Journal of Neuroscience*, *29*, 106–117.

West, R. W. (1976). Light and electron microscopy of the ground squirrel retina: Functional considerations. *Journal of Comparative Neurology*, *168*, 355–378.

West, R. W. (1978). Bipolar and horizontal cells of the gray squirrel retina: Golgi morphology and recepor connections. *Vision Research*, *18*, 129–136.

Yasuda, R., Nimchinsky, E. A., Scheuss, V., Pologruto, T. A., Oertner, T. G., Sabatini, B. L., & Svoboda, K. (2004). Imaging calcium concentration dynamics in small neuronal compartments. *Science STKE*, *2004*, pl5.

Zandt, B.-J., Liu, J. H., Veruki, M. L., & Hartveit, E. (2017). AII amacrine cells: Quantitative reconstruction and morphometric analysis of electrophysiologically identified cells in live rat retinal slices imaged with multi-photon excitation microscopy. *Brain Structure and Function*, *222*, 151–182.

Zandt, B.-J., Veruki, M. L., & Hartveit, E. (2018). Electrotonic signal processing in AII amacrine cells: Compartmental models and passive membrane properties for a gap junction-coupled retinal neuron. *Brain Structure and Function*, *223*, 3383–3410.

How to cite this article: Fournel, R., Veruki, M. L., & Hartveit, E. (2022). Digital reconstruction and quantitative morphometric analysis of bipolar cells in live rat retinal slices. *Journal of Comparative Neurology*, *530*, 1700–1728.
https://doi.org/10.1002/cne.25308